Localized Surface Plasmon Resonance: Single Particle to Ensemble Binding Measurements.

By

Jamie Nicholas Kulp

A dissertation submitted in partial satisfaction of the
Requirements for the degree of
Doctor of Philosophy
In
Chemistry
in the
Graduate Division
of the
University of California, Berkeley

Committee in charge:

Professor Marcin Majda, Chair
Professor Jay T. Groves
Professor Matthew Francis
Professor Stuart Linn

Fall 2014

Abstract

Localized Surface Plasmon Resonance: Single Particle to Ensemble Binding Measurements.

by

Jamie Nicholas Kulp

Doctor of Philosophy in Chemistry

University of California, Berkeley

Professor Marcin Majda, Chair

Plasmonic nanoparticles are an emerging technology, which demonstrates immense utility in the field of sensitive, label-free, molecular detection assays. Plasmonic nanoparticles exhibit a physical phenomenon known as Localized Surface Plasmon Resonance or LSPR. LSPR is a phenomenon based on the collective oscillations of free, surface electrons in certain metals such as silver and gold. The surface electrons couple to incident light at a specific frequency corresponding to the resonance frequency of these surface electron's oscillations. These oscillations scatter the incident light at the resonant frequency with a very high efficiency. The frequency of these oscillations and the scattered light is not only dependent on physical characteristics of the particles, such as their material composition, geometric shape and size, but also on the refractive index of both the particle and the surrounding medium in which the particles are located. Changes in the refractive index at the interface between the particle's surface and the surrounding medium, is the physical basis of analytical methods utilizing plasmonic nanoparticles. The sensitivity of the LSPR frequency to the surrounding medium's refractive index allows for the ability to observe changes in the refractive index at the particles surface due to molecular binding events. The monitoring of changes in the refractive index is accomplished by analyzing the peak LSPR frequency as a function of the refractive index at the surface interface of the particle and the surrounding medium. As molecular binding events occur at the surface interface between the particle and the surrounding medium, an increase in the local refractive index occurs. This increase in the local refractive index is accompanied by a red shift in the maximum LSPR wavelength of the scattered light. By monitoring changes in the maximum wavelength of scattered light, a calibration curve can be constructed, which relates the changes in the LSPR frequency to changes in the local refractive index at the particles surface. Changes in refractive index are ultimately related to a change in the mass of absorbed particles at the particle's surface due to molecular binding.

There are various instrumental methods that have been shown to be capable of detecting these refractive index changes at the plasmonic particles surface. These methods include solution-based ensemble techniques, as well as single particle

scattering measurements. Solution-based ensemble measurements commonly utilize UV-Visible spectrophotometers, but can also include the use of the backscattering interferometer. Single particle methods are predominately performed using the dark field scattering microscopy. The dark field scattering microscope is ideal for single particle measurements on plasmonic nanoparticles due to the particles remarkably high scattering coefficients relative to their geometrical size. The dark field scattering microscope also has relatively low background noise, which is particularly important for experiments on the single particle level where the signal-to-noise ratio must be maximized. Single particle dark field scattering methods involve the coupling of a dark field scattering microscope with a spectrometer in order to collect and analyze the scattered light of individual nanoparticles. The limitations and benefits of each of these experimental designs are discussed further in the body of this dissertation. Briefly, solution-based assays offer the benefit of being performed in colloidal suspensions of nanoparticles without the need to utilize specialized surface chemistry as a means to immobilize the particles to the underlying substrate. Solution-based measurements are also compatible, in most situations, with instrumentation that is commonly found in laboratories. As a result of the compatibility of solution-based measurements with common laboratory instruments, such as the UV-visible spectrometer, measurements do not generally require dedicated, specialized instrumentation. This of course is not universally true as will be seen with experiments are performed using the backscattering interferometer. However, many examples of solution-based assays utilizing more common laboratory instrumentation are now available in the literature. Despite these advantages, solution-based colloidal measurements are ensemble measurements and due to the statistical nature of these measurements, individual, unique features that may occur on the single particle level are obscured due to the averaging of many particles contribution to the collected signal. To overcome this statistical limitation, single particle assays have been developed. Most notably among these single particle experiments is the use of dark field scattering microscopy, coupled with spectroscopic measurements of the scattered light to examine the optical properties of individual nanoparticles. While this platform has shown that it is possible to interrogate individual particles, as well molecular binding events occurring at the surface of the particles, there are a few technical drawbacks to this method as well. The first of these technical drawbacks is the need to immobilize the particle onto the underlying substrate. This is to prevent random Brownian motion of the particles when performing experiments in aqueous environments. When observing the particles in a vacuum or air environment this need is not as rigorous as the electrostatic interactions between the particle and the underlying substrate are sufficient to immobilize the particle during measurements. In order to explore binding events occurring in aqueous systems, which include receptor-ligand binding, DNA-DNA base pairing and other solution-based molecular recognition events, it is necessary to develop a method of immobilizing the particle to the surface of the underlying substrate utilizing surface chemistry techniques. In this dissertation it is shown that the use of the supported lipid bilayer is a very effective and versatile means of accomplishing this immobilization of the particle to the underlying substrate used in dark field microscopy. This can be accomplished by incorporating biotin-functionalized lipids into the composition of a supported lipid bilayer formed on the particles, as well as the supported bilayer formed on the underlying substrate. The formation of a supported

lipid bilayer containing a fraction of biotin-functionalized lipids on the underlying substrate, as well as the nanoparticle, it is possible to tether the particles to the substrate surface through streptavidin-biotin molecular interactions. This proves to be a robust and simple method of immobilizing particles to a substrate capable of supporting the formation of a supported lipid bilayer. Silica oxide or glass is a material, which allows for the spontaneous formation of a supported lipid bilayer from single unilaminar vesicles. Presented here is the synthesis of cubic geometry nanoparticles that are surrounded with a thin silica shell of nanometer thickness. This thin silica shell allows for the spontaneous formation of a supported lipid bilayer on individual nanoparticles. This feature facilitates the immobilization of the particles for studies using the dark field scattering microscope. Nanoparticle-based analytical platforms, regardless of being implemented on the single particle level or using colloidal, solution-based ensemble measurements, offer a very robust and sensitive, label-free analytical technique for quantify molecular binding events occurring at the particle’s surface.

Acknowledgements

- **My undergraduate research advisor – Dr. Chul-Hyun Kim**. Dr. Kim was very influential in my development as a young scientist during my undergraduate education at California State University, East Bay. I am forever grateful for the freedom and level of respect he gave me as a young scientist. The many hours of cultivating cells, purifying proteins and synthesizing RNA sequences using the T7 RNA polymerase in-vitro platform will always be fond memories.
- **Dr. Joy Andrews** – While Dr. Andrews was not my research advisor, I had the pleasure of sharing a hallway with her laboratory. Her laboratory was across the hall from Dr. Kim's and this proved very fortuitous. I was able to not only interact personally with Dr. Andrews, but her advice and tutelage regarding my scientific career was always valued and very insightful.
- **Dr. Marcin Majda** – Marcin is the reason I am in graduate school today. I have to say my initial experience with graduate school was very poor and I often thought of leaving. I am forever grateful to Marcin for showing me how exciting, demanding and rewarding research can be in the field of chemistry. I always will respect the level of detail and scrutiny Marcin brings to his scientific perspective. He pushed me at the times I wanted to quit and cheered me up when I needed a helping hand. He showed me that I could accomplish my goals if I keep focused and work hard regardless of challenges and obstacles that arise. I am sad, that due to circumstance beyond our control, I was not able to finish the project in Marcin's laboratory. I still have hope that someday the competitive bead assay will come to its mature completion! Thank you Marcin for everything you have taught and shared with me during my time at Cal. You are truly one of UC Berkeley's most valued professors and I am proud to have been one of your students.
- **Groves Laboratory** – Although I joined the Groves laboratory late in my graduate career, those years were very special. The interactions I had with all of my lab mates will also be very fond memories to me and hopefully I will remain in contact with all of you once my time has come to move on! I do wish I had more time to interact with Young-Kwang. I always enjoyed our talks regarding plasmonics and the experience Young-Kwang possessed with these particles. Thank you Young-Kwang for teaching me about nanoparticles and helping me learn about dark field microscopy as well.
- **MY PI – Dr. Jay Groves** – I would like to thank Jay for the chance to work in his lab and learn about and develop the plasmonic nanocube project. This was another event I did not foresee in my career when I began at Cal. Jay was kind enough to arrange for me to work on the project following my qualifying exam. I only wish I had more time to explore the

exciting area of LSPR based platforms. Jay was also always one to see what no one else saw and give advice that I feel no one else would give. He has such a unique perspective on science and I am grateful I was exposed to his ideas and approach to science. Through Jay I have had the opportunity to develop, yet another level of my scientific training and my perspective on pursuing a scientific career.

- **My Family** – First my Mom for supporting me always. She was always willing to help me, whether just to talk or in any other way I needed. I know it was not always easy for either of us, but you always supported me and encouraged me to keep working hard. If only I had listened to you when I first selected my research advisor I might have met Jay and Marcin earlier! I guess your mother is usually right. I hope I can repay you for everything you have done for me someday. Second my Dad, even though he is very quiet about things I know he always supported me and always was proud of what I have done with my life. I think a great deal of my interest in science and technology I gained from you. I remember when I was young my brother Mike and I would travel with my Dad to Philadelphia to attend computer programming classes on Saturday mornings. I think these early experiences with technology stayed with me and helped me decide what to pursue in my life. Also to my brother Mike for playing hockey with me on Thursday nights. While this is unrelated to science it was a great time always and I think something I greatly needed to stay focused and normal when the rest of my life was not some common place. To PJ, I just wish you were around to see this also. Perhaps someday.
- **My old friends – Joey and Albert**. I have known you both since I was young and I am truly blessed to have such great friends in my life. I feel like you are both brothers to me. Joey I thank you for years of things like the talks we had daily to “cleaning the garage” as well as our endeavors in brewing. I hope now that I am free of grad school we can start spending more time together again! Albert you were always pushing me as a kid and sometime I might have resisted, but I think you never wanted anything but to help me improve and I am forever grateful to you for this. I know that there is no one in this world like you and I am very thankful I can call you a friend. I am looking forward to the years to come with you, Erin and Solei! Oh and of course our Sunday bouldering sessions!
- **Lesley Kana** – For Lesley you are the newest person in my life and yet one of the closest. I am very grateful the universe brought you into my world. You also keep me focused, fed and cheerful! I know you might not think you do these things since you are so humble, but you do and I always remember what you bring to my life! I am very excited about what life will bring us together!
- **Dr**. **Stuart Linn** – I wanted to thank Stuart for all the time and patience he showed to me during my qualifying examination preparation as well as during my dissertation review process.

Table of Contents

List of Figures

Chapter 1

Introduction: Bio-analytical Methods, Immunological Assays, Surface Plasmon Resonance and Localized Surface Plasmon Resonance.

Chapter 1.1: Introduction to Bio-analytical Methods

Bio-analytical chemistry is a rapidly growing field in modern analytical chemistry. The ability to detect biological molecules, in both a qualitative and quantitative manner, is of critical importance in a variety of fields ranging from pharmaceutical drugs production, to diagnostic medicine and basic research in biochemistry. The use of bio-analytical chemistry in these fields involves anything from the quantification of bio-molecules in a patient's blood sample, to understanding the kinetics of bio-molecular recognition pathways between a receptor and ligand. Bio-analytical chemistry provides a physical means of not only quantifying molecular concentrations of solutions, but also of obtaining physical parameters, such as kinetic rates and equilibrium constants. The characterization of these physical parameters involved in bio-molecular recognition is of fundamental importance in fields like biochemistry, and pharmaceutical drug design. The affinity of molecules for their molecular receptors is a key parameter that determines the efficacy of a drug.[1,2] The understanding of the kinetics and affinity of these molecular systems provides a means of comparing various drugs' efficacy in both a qualitative and quantitative manner.

The focus of this dissertation will be on the optical properties of plasmonic nanoparticles and how these properties can be utilized in the development of quantitative, label-free analytical assays. However, many of the techniques developed for the immunological assays are utilized in the preparation of the nanoparticle surface. These modifications are necessary so that the particle is capable of capturing the molecule of interest in a very selective and specific manner with very little non-specific interactions for other molecules present in a sample. A brief review of some of these immunological techniques will first be covered. This will be followed by a background introduction to the phenomenon of Surface Plasmon Resonance and Localized Surface Plasmon Resonance in order to compare the traditional immunological assay to these newer label-free techniques.

1.2 Immunological Assays.

A great number of modern analytical techniques are based on the principles of the immunoassay. All immunochemical techniques are based on the specific, non-covalent interaction between antigens and specific antibodies.[3] A large variety of immunoassays exist, which range from the Enzyme Linked Immunosorbent Assay (ELISA), the Radioimmunoassay (RIA), and the precipitation assays.[3] The ELISA in particular illustrates the molecular basis of the immunoassay very well. The ELISA makes use of the very specific affinity of antibodies for one particular antigen molecule. This allows for the capture of an antigen by the antibody in a very specific manner with very little cross-reactivity between other foreign molecules.[1] The exploitation of the antibody-antigen interaction is a very useful technique, where the antibody is used as a capture agent for a specific antigen molecule and allows the design of analytical assays with a high degree of selectivity towards one and only one molecule due to the

incredibly high specificity of antibodies towards their antigens.[1] Modern molecular biology techniques have advanced to the point, that there exist libraries of antibodies that are specific for particular epitopes on each antigens. This allows for the screening and quantification of a large number of antigen molecules utilizing the immunoassay's principles of detection.[1] The generic dissociation reaction and the associated dissociation constant (K_d) for the ligand-receptor dissociation reaction utilized in the immunoassay's capture of the ligand of interest by its associated receptor, are shown in equation 1.1 and 1.2 respectively.

$$[\mathbf{Ligand-Receptor}] \longleftrightarrow [\mathbf{Ligand}][\mathbf{Receptor}] \quad \textbf{(1.1)}$$

$$\mathbf{K_d} = \frac{[\mathbf{Ligand}][\mathbf{Receptor}]}{[\mathbf{Ligand-Receptor}]} \quad \textbf{(1.2)}$$

In order to appreciate the importance of the ligand-receptor or antibody – antigen interaction and its role in the ELISA, it is necessary to understand the physical mechanism behind the ELISA. The platform generally consists of a solid support that allows for the immobilization of the antibody to its surface. This is accomplished through the use bio-conjugation chemistry techniques that exploit the reactivity of molecular moieties present on the surface of amino acids within the antibody, to a variety of reactive functional groups which can be incorporated into the substrate's surface.[4] The reactive groups found in antibodies include aldehydes, primary amines, carboxylic acids and sulfhydryl groups.[4] The basic concept is to tether the antibody to a solid support through a covalent bond formed between a reactive functional group, incorporated on to the solid support, and a reactive group present on the antibody surface. The choice of the immobilization technique can have an effect on the actual affinity of the receptor for the ligand of interest depending on the location of the reactive group on the antibody, which tethers the molecule to the substrate.[4] The antibody tethered to the solid support surface is chosen specifically to serve as a capture agent for one antigen of interest, providing the ability of the ELISA to bind in a very selective manner to the antigen of choice. This primary antibody will recognize a specific region or epitope on the antigen molecule. Once the antibody is bound to the surface of the solid support, it is exposed to the antigen of interest where the two molecules will bind together to form an antibody-antigen complex at the surface of the solid support. This complex is held together through the non-covalent interactions of one of the antigen's epitopes with the antibody. The initial antibody, which is tethered to the substrate's surface, is referred to as the primary antibody. Following extensive washing of the sensors surface, the antibody-antigen complex is then exposed to a secondary antibody that is chosen such that it interacts with the antigen in a very selective manner as well, but this interaction is with a different epitope or region of the antigen than the primary antibody that is tethered to surface of the solid support.[1] This secondary

antibody is labeled with a range of molecules, which include labels such as fluorescent dyes and enzymes through bio-conjugation chemistry similar to that used to tether the primary antibody to the solid support.[1] Once this secondary antibody binds to the primary antibody – antigen complex, we have what can be visualized as a antibody-antigen-antibody sandwich at the surface of the solid support. The role of the labeled, secondary antibody is to provide a detectable physical signal, which indicates that the antigen of interest has been captured at the sensor's surface. In order to quantify the amount of antigen captured, a calibration curve is generated correlating the physically measurable signal from the labeled, secondary antibody to the amount of antigen captured. A common example of a physical signal used in these calibrations is the fluorescent intensity from a fluorescently labeled secondary antibody.[3] The intensity of the fluorescent signal can be correlated to the amount of antigen captured at the sensors surface. If instead of utilizing a fluorescent probe bound to the secondary antibody, the secondary antibody is tethered to an enzyme, we can determine the amount of antigen captured by the sensor by measuring the production of a particular compound produced by the enzyme. For example, if the secondary antibody is bound to a horseradish peroxidase enzyme (HRP), then we can monitor the enzymatic breakdown of hydrogen peroxide in a given period of time. The rate of this degradation of the hydrogen peroxide by the horseradish peroxidase is related to the amount of the enzyme present at the sensor's surface. This rate of hydrogen peroxide degradation can be correlated to the amount of captured antigen in a manner analogous to the method used for a fluorescently labeled secondary antibody. The reaction of the enzyme can be monitored with a variety of techniques including electrochemical methods and spectroscopic techniques.

1.3 Surface Plasmon Resonance (SPR)

The ELISA platform is a robust and sensitive method for quantifying bio-molecular interactions. However, the ELISA suffers from a number of drawbacks that illustrates the need for the development of new methods in bio-analytical chemistry. One major drawback of the ELISA is the need for both a primary and a secondary antibody. These both must possess a very high affinities for the antigen, but this affinity must be for a different region of the antigen molecule in a manner that does not affect the binding the other antibody to the antigen.[3] The need to have two different antibodies, with affinities for different epitopes on the antigen, is a requirement that makes the detection of some molecules difficult using the ELISA. The discovery of Surface Plasmon Resonance (SPR) has proven to be an attractive alternative to the ELISA. However, as we will see SPR also suffers from some technical drawbacks.[5,6,7] Surface Plasmon Resonance is an optical method, which measures the refractive indexes of very thin layers of material adsorbed on a metal.[8] When illuminated with white light, a small portion of the incident light is coupled to the electrons at the surface and results in a decrease in the intensity of the reflected light at a particular frequency.[8] When a metal surface is irradiated with electromagnetic radiation of the appropriate

frequency, a coherent oscillation of the metal's conduction electrons is induced orthogonal to the propagation direction of the light.[8] These oscillations occur at a specific frequency that is dependent on both the real dielectric constant of the metal, as well as the dielectric constant of the surrounding medium. This resonance condition requires that the incident light's frequency matches the natural oscillatory frequency of the surface electrons in the metal.[8] Since these are surface electrons and are located at the interface of the metal and the surrounding medium, the frequency of these oscillations very sensitive to changes in the refractive index close to the surface of the metal.[8] The SPR technique is based on the fact that, at certain conditions, surface plasmons on a metallic film can be excited by photons, thereby transforming a photon into a surface plasmon. The frequency of this plasmon depends on the refractive index of the adsorbate. Small changes in the refractive index of the surrounding medium manifest as changes in the frequency of light that is coupled to the surface electrons.[8] A spectrum of white light coupled to the surface of the metal will show a narrow band of light being absorbed or scattered, which corresponds to the plasmon frequency of the oscillations of the surface electrons on the metal. Since this frequency is dependent on both the real part of the dielectric of the metal, as well as the surrounding medium's dielectric constant, it is sensitive to changes in the surrounding medium's dielectric constant. The dielectric constant of a material is related to its' refractive index by the relationship shown in equation 1.3.[9]

$$\boldsymbol{\varepsilon = n^2} \qquad \textbf{(1.3)}$$

In equation 1.3, *n,* is the refractive index of the material and $\boldsymbol{\varepsilon}$ is the associated dielectric constant. Changes in the refractive index of a material are related to with changes in the material's dielectric constant. This relationship between refractive index and dielectric constant serves as the physical means of detecting binding in SPR assays. By the monitoring the frequency of light, which is absorbed or scattered at the metals surface, changes in the refractive index due to molecular binding events are detected.

The design of an SPR experimental platform is very closely related to the design of the ELISA. In SPR, a solid support such as a glass slide is coated with a very thin layer of metal, such gold or silver. Capture antibodies are tethered to the glass slide on the opposite side of the glass from the thin gold or silver layer. The gold layer is separated from the antibody layer by a thin strip of silica glass. The conjugation of the antibodies to the silica support uses the same bio-conjugation chemistry techniques as used in the production of the ELISA platform. However, the advantage of the SPR platform over the ELISA is that only the primary capture antibody is needed in order to detect molecular binding events. The signal provided by the labeled secondary antibody is now no longer needed. The signal in SPR is based on the changes in the refractive index at the surface of the sensor as the antigen is captured by the antibody.[8] A calibration curve can be generated, which relates known changes in the mass adsorbed at the surface of the sensor, to changes in refractive index and its associated shift in the plasmonic frequency. As an increasing number of antigen molecules are

captured by the antibodies at sensor's surface, the resonant frequency of the will experience a red shift. SPR is a very reliable and robust method of quantifying bio-molecules in solution, as well as a technique for characterizing the kinetics of the on and off rates of receptor-ligand interaction. While the SPR platform has the advantage of not requiring a secondary antibody for detection and quantification and so is a truly label-free detection platform, it does suffer from a number of drawbacks. The first of these drawbacks is the requirements of the optical setup. The basic requirement is the establishment of a total internal reflection optical setup, where a portion of the light is propagating parallel to the surface setting up an evanescent field and allowing for the correct spatial coupling of the incident light to the oscillations of the surface electrons.[14] This requires precise alignment of the optical components, as well as a dedicated optical arrangement.[5,6,7,8] Figure 1.1 is a schematic of a standard SPR experimental arrangement.

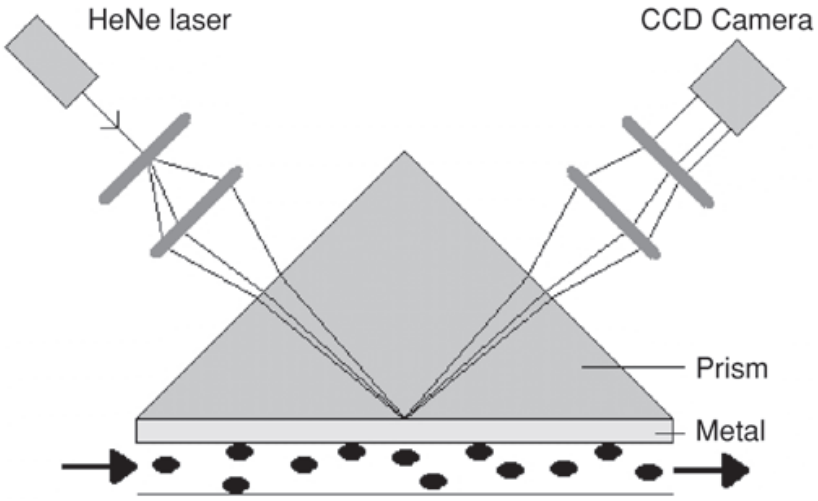

Figure 1.1 Surface Plasmon Resonance Experimental Arrangement. This image was adapted from reference 8.

A major additional drawback of the SPR experimental regime is the bulk sensitivity of the surface plasmon resonance to changes in the refractive index. This sensitivity to changes in the refractive index extends hundreds of nanometers into the solution rather than being localized to the surface of the gold coated slide for most SPR arrangements.[8] The sensitivity to changes in the refractive index, which extend hundreds of nanometers means that molecules need not be captured at the surface interface in order to induce a change in the resonant frequency of the SPR signal. This can be accounted for by proper control experiments, however a more optimal situation would be a sensor whose sensitivity is localized to a small distance from the sensors surface.

1.4 Localized Surface Plasmon Resonance (LSPR)

While SPR deals with the oscillations of the surface electrons in a bulk substrate as described above, Localized Surface Plasmon Resonance or LSPR deals with the oscillation of surface electrons for particles typically smaller than 100 nanometers. With Localized Surface Plasmon Resonance, light interacts with particles which are smaller than the incident wavelength.[10] This situation results in a plasmon that oscillates around the nanoparticle at its resonance frequency referred to as the Localized Surface Plasmon Resonance or LSPR.[10] Materials that possess a negative real and small positive imaginary dielectric constant are capable of supporting a surface plasmon resonance either SPR or LSPR.[10] This resonance is a coherent oscillation of the surface conduction electrons excited by electromagnetic radiation. When a particle of radius a, is illuminated by a wavelength λ where a, is much smaller than λ, the electric field surrounding the particle can be treated as static.[10] Figure 1.2 illustrates the general difference in the electric field produced in a small metallic nanoparticle relative to that produced by Surface Plasmon Resonance.[10] As was stated the wavelength of the incident light is large compared to the size of the metallic nanoparticle leading to a uniform electric field which surrounds the entire nanoparticle.

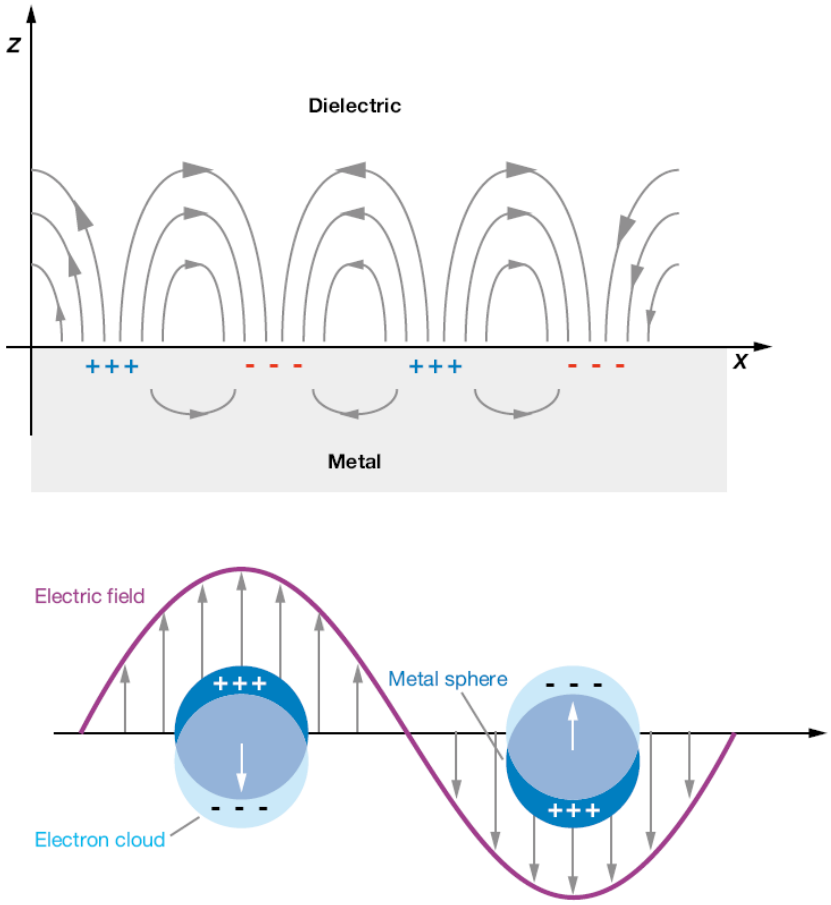

Figure 1.2 Electric Field Diagram for SPR and LSPR. This illustration demonstrates the electric field associated with surface plasmon resonance (SPR)(top) and local surface plasmon resonance (LSPR)(bottom), respectively. Figure adapted from reference 10.

The apparent static electric field makes it possible to solve Maxwell's equations using a quasi static approximation.[10,11,12] This assumption leads to the following result for the electromagnetic field surrounding the particle.[10]

$$\boldsymbol{E_{out}(x,y,z) = E_o\hat{z} - \left[\frac{\varepsilon_{in}-\varepsilon_{out}}{(\varepsilon_{in}+2\varepsilon_{out})}\right] a^3 E_o \left[\frac{\hat{z}}{r^3} - \frac{3z}{r^3}(x\hat{x}+y\hat{y}+z\hat{z})\right]} \qquad \textbf{(1.4)}$$

The term ε_{in} in equation 1.4 is the dielectric constant of the metallic nanoparticle, while ε_{out} is the dielectric constant of the surrounding medium. In general the dielectric constant ε_{in} of the metallic nanoparticle is wavelength dependent.[10] The electromagnetic field surrounding a particle is enhanced, when the dielectric constant ε_{in} of the metallic nanoparticle is nearly equal to twice the negative value of ε_{out}. This criterion establishes the conditions of resonance for the nanoparticle. It has been determined that for both gold and silver metallic nanoparticles this resonance frequency falls within the visible region.[10] The

radius of the nanoparticle also affects the strength of the electric field outside of the metallic nanoparticle, as can be seen from the second term in brackets. The results, as shown in equation 1.4, indicate that when the conditions for resonance are met, there is an enhancement of the electric field surrounding the nanoparticles relative to the incident field.

The extinction spectrum of the nanoparticles, which is a combination of both absorption and scattering of light by the particle, can also be calculated. The extinction coefficient of the nanoparticle is shown in equation 1.5.[10,13,14]

$$\mathbf{E}(\boldsymbol{\lambda}) = \frac{\left(\mathbf{24\pi^2 N a^3 \varepsilon_{out}^{3/2}}\right)}{\boldsymbol{\lambda}\mathbf{ln(10)}} \left(\frac{\boldsymbol{\varepsilon_i}(\boldsymbol{\lambda})}{(\boldsymbol{\varepsilon_r}(\boldsymbol{\lambda}) + \boldsymbol{\chi\varepsilon_{out}})^2 + \boldsymbol{\varepsilon_i}\mathbf{i}\,(\boldsymbol{\lambda})^2}\right) \quad \textbf{(1.5)}$$

In equation 1.5, $\varepsilon_i(\lambda)$ and $\varepsilon_i(\lambda)$ are the imaginary and real components of the dielectric constant for the metallic nanoparticle respectively. Both components of the dielectric constant of the nanoparticle are wavelength dependent. $\mathbf{X}$ is a term that accounts for the geometrical aspect ratios and can vary with values from values of 2 for spherical particles to values as high as 20 for other high aspect ratios.[10,15]. The value for all geometries other than spheres and spheroids must be approximated.[10,15] These approximation methods include discrete dipole approximations and finite-difference time domain approximations.[10,16,17,18,19,20,21] Using these various methods allows for the determination of the LSPR scattering maximum wavelength (λ_{max}) for particles of shapes other than a sphere or spheroid.[10] This LSPR wavelength maximum is sensitive to the refractive index of the surrounding medium. Changes in the surrounding medium's refractive index will lead to changes in the maximum scattered wavelength of the metallic nanoparticle.[10,22,23] This change can be a result of being immersed in a new medium possessing a different refractive index or by the absorption or desorption of a molecular layer at the interface of the metallic nanoparticle and the surrounding medium. This sensitivity of maximum wavelength of light scattered by the plasmonic particle to changes in the refractive index at the particles surface, can be modeled using the equation 1.6.[10]

$$\Delta\boldsymbol{\lambda}(\boldsymbol{max}) = \boldsymbol{m}(\Delta\boldsymbol{\eta})\,[\mathbf{1} - \mathbf{exp}\,(-\frac{\mathbf{2}\boldsymbol{d}}{\boldsymbol{I_d}})] \quad \textbf{(1.6)}$$

In equation 1.6, m is a factor describing the degree to which the maximum wavelength of scattered light will shift as a function of changes to the refractive index of the surrounding medium. The remaining terms in equation 1.6, Δn, d, and I_d, represent the change in the refractive index at the interface, the thickness of the adsorbed layer of matter at the particles surface, and the surrounding medium and the characteristic decay length of the electric field enhancement surrounding the metallic nanoparticle, respectively. The electric field enhancement for metallic nanoparticles is very short range with length scales of approximately 5-30 nanometers.[10] The short range electric field enhancement is a significant improvement of LSPR's sensitivity to refractive index changes in comparison to the bulk sensitivity of SPR, which extended hundreds of

nanometers beyond the plasmonic surface.[10] The short range nature of LSPR's electric field enhancement ensures that, changes in the refractive index affecting the maximum wavelength of scattered light by the particle's plasmons, are a result of near field changes in the refractive index.

In addition to the effective response m of the metallic nanoparticles as found in equation 1.6, an additional relationship termed the figure of merit (FOM), is often quoted as a means of quantifying the sensitivity of various metallic nanoparticles of different geometries.[10] This figure of merit allows for nanoparticles of various shapes to be directly compared.[10] The FOM is defined as equation 1.7.[10]

$$\mathbf{FOM} = \frac{\mathbf{m(nm * RIU^{-1})}}{\mathbf{FWHM\ (nm)}} \qquad \textbf{(1.7)}$$

In equation 1.7, m is the response of the particles to changes in the refractive index with units of nanometers per refractive index units (RIU). FWHM is the full width at half maximum of the corresponding LSPR peak. Dividing the response factor m, by the FWHM allows for the normalization of various shaped nanoparticles response to changes in the refractive index at their surface.[10]

Although SPR spectroscopy currently dominates commercial instrumentation, LSPR spectroscopy offers many of the same advantages for sensing and spectroscopy experiments, along with several additional benefits.[10] First and foremost is that in most cases LSPR experiments do not require dedicated optical arrangements in order to couple the incident light to the surface electrons of the plasmonic nanoparticles. Often LSPR experiments can be conducted in common laboratory instruments, which include the UV-Vis spectrophotometers and dark field microscopy. In addition, LSPR based plasmonic nanoparticle assays do not suffer from the bulk solution sensitivity to changes in the refractive index far away from the particles surface that SPR systems do. SPR experiments are sensitive to refractive index changes in solution that extend hundreds of nanometers above the plasmonic metal/solution interface, while LSPR plasmonic nanoparticles are only sensitive to changes that extend into the solution a distance of 5-30 nanometers.[10] The short range sensitivity of plasmonic nanoparticles greatly reduces effects due to bulk changes in the surrounding medium's refractive index. This allows the interrogation of changes in the refractive index that occur only at the interface between the nanoparticle surface and solution, such as the formation of thin molecular layers of absorbed material.

1.5 Literature Cited

1. Wild D., *The Immunoassay Handbook,* 3rd ed, Elsevier, Amsterdam, 2005. [general immunoassay information]
2. Diamandis E.P. and Christopoulos T.K. *Immunoassay*, Academic Press, Inc., San Diego, 1996
3. Chu F.S., Ekins R., *Protein Arrays, Biochips and Proteomics: The Next Phase of Genomic Discover*, Elsevier Amsterdam, 2003.
4. Hermanson G. *Bioconjugate Technicques, 3rd ed, Elsevier, Amsterdam, 2013.*
5. Myszka D.G., Current Opinion in Biotechnology, 1997, 8, 50.
6. Rich R.L. and Myszka D.G., Current Opinion in Biotechnology, 2000, 11, 54.
7. Kyo M., Kazue U.-A., and Koga H., Analytical Chemistry, 2005, 77, 7115.
8. Pattnaik P., Applied Biochemistry and Biotechnology, 2005, 126, 79
9. Yonzon C.R., Jeoung E., Zou S., Schatz G.C., Mrksich M., Van Duyne R.P., Journal of American Chemical Society, 2004, 126, 12669-12676.
10. Willits K., Van Duyne R.P., Annual Review of Physical Chemistry, 2007, 58, 267.
11. Schatz GC, Young MA, Van Duyne RP. 2006. Electromagnetic mechanism of SERS. In *Surface-Enhanced Raman Scattering: Physics and Applications*, ed. K Kneipp, Moskovits >, H Kneipp, pp. 19–46. Berlin: Springer-Verlag.
12. Kelly KL, Coronado E, Zhao L, Schatz GC. Journal of Physical Chemistry, 2003, B 107:668–77.
13. Bohren CF, Huffman DR. 1983. *Absorption and Scattering of Light by Small Particles*. New York:Wiley. 530 pp.
14. Mie G. 1908. Contributions to the optics of turbid media, especially colloidal metal solutions. *Ann. Phys.* 25:377–445.
15. Link S, El-Sayed MA. 1999. Spectral properties and relaxation dynamics of surface plasmon electronic oscillations in gold and silver nano-dots and nano-rods. *J. Phys. Chem. B* 103:8410–26.
16. Draine BT, Flatau PJ. 1994. Discrete-dipole approximation for scattering calculations. *J. Opt. Soc. Am. A* 11:1491–99
17. Jensen TR, Kelly KL, Lazarides A, Schatz GC. 1999. Electrodynamics of noble metal nanoparticles and nanoparticle clusters. *J. Cluster Sci.* 10:295–317
18. Yang W, Schatz GC, Van Duyne RP. 1995. Discrete dipole approximation for calculating extinction and Raman intensities for small particles with arbitrary shapes. *J. Chem. Phys.* 103:869–75
19. Taflove A. 1995. *Computational Electrodynamics: The Finite-Difference Time Domain Method*. Boston: Artech House
20. Novotny L, Bian RX, Xie XS. 1997. Theory of nanometric optical tweezers. *Phys. Rev. Lett.* 79:645–48
21. Bian RX, Dunn RC, Xie XS, Leung PT. 1995. Single molecule emission characteristics in near-field microscopy. *Phys. Rev. Lett.* 75:4772–75

22. Haes AJ, Van Duyne RP. 2002. A nanoscale optical biosensor: sensitivity and selectivity of an approach based on the localized surface plasmon resonance of triangular silver nanoparticles. *J. Am. Chem. Soc.* 124:10596–604
23. Jung LS, Campbell CT, Chinowsky TM, Mar MN, Yee SS. 1998. Quantitative interpretation of the response of surface plasmon resonance sensors to adsorbed films. *Langmuir* 14:5636–48

Chapter 2

Synthesis of Cubic Plasmonic Nanoparticles

2.1 Introduction

The synthesis of various shaped plasmonic nanoparticles is a topic which receives a great deal of interest as the extinction spectrum of nanoparticles is greatly determined by the geometrical shape of the particle itself.[1] Sub-wave length silver nanoparticles display a variety of unrivaled optical properties in the visible and near-IR regime, including scattering cross-sections that are orders of magnitude higher than the fluorescence emission from organic dyes, as well as intense local amplification of electromagnetic fields.[1] For silver particles with diameter $d << \lambda$, where λ is the wavelength of the incident light, a single dipolar plasmon mode is allowed.[1] Principally, polyhedral shapes with well-defined facets and corners are predicted to have distinct scattering signatures in addition to scattering efficiencies that are orders of magnitude higher than those of their spherical counterparts.[1] Specifically cubic shaped plasmonic nanoparticles have been shown to exhibit not only a dipole LSPR peak, but additional higher order resonances associated with the sharp edges and corners of these structures.[1]

The polyol method, first developed Sun and Xia[2], has been adapted by Tao, Sinsermsuksakul, and Yang[1], and has been shown to produce very uniform size distribution of particles of a specific geometry. The geometry of the particle produced is dependent on the reaction conditions. Cubic silver nanoparticles can be synthesized using the polyol method. In the polylol method a silver metal salt is reduced by a diol solvent at near-reflux temperatures in the presence of a polymeric stabilizing agent.[1,2] With precise control over the reaction conditions that will be detailed in the remainder of this chapter, a colloidal suspension of monodisperse cubic silver nanoparticles can be produced. These cubic structures have diameters on the order of 80-100nm.[1] In addition the cubes have been shown to exhibit sharp corners and edges which give rise to the higher order resonance modes mentioned above.[1] These higher order resonance modes associated with these edges and corners ultimately will be seen to exhibit higher figures of merit than the much broader dipolar resonance peaks due to their narrow band widths.

2.2 Reagents and Materials

The polyol synthesis method is a single pot solution based synthesis. The reaction uses 1,5-pentanediol (97%) obtained from Alpha Aesar, $CuCl_2 \cdot H_2O$ Fisher Scientific, $AgNO_3$ Alfa Aesar Premion 99.995% metal basis, Polyvinlypyrrolidone (PVP) M.W. 55,000 from Sigma Aldrich, ethanol absolute (200 proof) from Fisher Scientific, Silicone oil (-50 to +200 degrees Celsius) from Sigma Aldrich, RET Control-VISC Kit, IKEA Hot Plate Stirrer (Stainless Steel), VWR, Kontes Bottom Boiling Flasks 100mL VWR, 47mm filters with glass support from Sigma Aldrich, #8 stopper from Sigma Aldrich, 1 L Vacuum Flask from Sigma Aldrich, and 5µm, 0.22µm and 0.45µm Millipore Filter membranes all with 47mm diameters from Sigma Aldrich. The reaction is extremely sensitive to the purity of the 1,5-pentanediol and it is recommended to use freshly opened

bottles of this reagent. In addition in this synthesis very little success was found when using reagents from any supplier other than Aesar Alfa. The remaining reagents appear to exhibit a higher tolerance from supplier to supplier and I have seen no difference in reaction based on the quality of various batches of these remaining reagents. An IKEA hot plate is needed along with a high temperature silicon oil bath. The silicon oil should be clean and lacking any particulate matter in order to maintain a consistent temperature bath. The control of the reaction temperature is critical as the rate of reaction and final morphology of the nanoparticles produced are very sensitive to small changes in the temperature.

2.3 Polyol Nanocube Synthesis

The synthesis of the cubic nanoparticles is again a single pot synthesis. The following solutions are prepared prior to beginning the reaction. This step will require at least 1 hour for all the reagents to dissolve completely. In addition the sonicator should be turned on with the temperature control set to 35 degrees Celsius before immersing the reagents to dissolve.

1. Round bottom flasks with stir bar should be cleaned with aqua regia for 1 hour, followed by 10 rinses with MilliQ water, and rinsed with ethanol then dried over night in an oven.
2. 0.080-0.085g of $CuCl_2 \cdot H_2O$ dissolved in 10mL of 1,5-pentanediol. Sonicate and vortex the solution occasionally until completely dissolved. This solution can be kept for future reactions done within the week.
3. A solution of 0.4g of $AgNO_3$ dissolved in 10mL of 1,5-pentanediol yielding a final concentration of 120mM $AgNO_3$. To this solution 35µL of the $CuCl_2 \cdot H_2O$ solution prepared in step 1 is added. This solution should also be sonicated and vortexed until the $AgNO_3$ is completely dissolved. The color of the solution will be light orange to yellow. This solution should be protected from light to prevent the reduction of the $AgNO_3$ salt.
4. 0.2g of polyvinlypyrrolidone (M.W. 55,000) is dissolved in 10mL of 1,5-pentanediol and sonicated and vortexed until completely dissolved.
5. A silicone oil bath should be heated on the IKEA hot plate to 180 degrees Celsius.

After completely dissolving all of the compounds listed above and bringing the silicone oil bath to the appropriate temperature, the reaction is ready to begin. The reaction will take approximately 20 minutes to complete. A stopwatch should be set to 20 minutes and used to monitor the timing of each injection of the reagents into the round bottom flask.

The reaction consists of the following steps:

1. Into a clean and dry 100mL round bottom flask, which was previously cleaned with aqua regia, 20mL of 1,5-pentanediol is added. The round bottom flask is then submerged approximately 1cm into the silicone oil bath and stirred at 300rpms. The depth of the flasks immersion into the oil bath can be monitored and changed depending on if the reaction is proceeding to quickly or slowly. The round bottom flask should be heated for 2 minutes prior to moving to the next step. Typically at this point a small amount of vapor will begin to condense on the walls of the round bottom flask. The depth and time of this step can be adjusted to higher or lower depending on how quickly reaction is proceeding. If the reaction is occurring too quickly then the flask can be heated for a shorter period of time and if the reaction is occurring too slowly then this time of initial heating can be increased.
2. Initially 250µL of the $AgNO_3$ solution prepared previously is injected into the flask, followed immediately by 250µL of the polyvinlypyrrolidone solution. Care should be taken that each injection does not run down the walls of the flask preventing condensation from being added to the reaction solution.
3. After 25 seconds, an additional 500µL of the $AgNO_3$ solution is injected followed immediately by 500µL of the polyvinlypyrrolidone solution. Again care should be taken to avoid having this solution run down the side of the reaction flask.
4. Subsequently every minute an additional 500µL of the $AgNO_3$ solution followed by 500µL of the polyvinylpyrrolidone solution will be added to the reaction flask until 20 minutes have passed.
5. After the reaction injections are complete the flask should be removed from the silicone oil bath and allowed to cool.
6. The reaction is then split evenly into 2, 50mL Falcon centrifuge tubes. Then 200-proof ethanol is added to a total volume of 50mL in each Falcon tube.
7. This solution should be centrifuged at 2900g for 1.5 hours. This is followed by removal of the supernatant and the subsequent suspension in either 1,5-pentanediol or 200-proof ethanol. The cubes may be stored up to one month in either the 1,5 pentanediol or 200-proof ethanol with very little sign of degradation.

Following the synthesis the cubes must be filtered further to remove any larger particles from the suspension. This will greatly improve the size distribution of the particles in solution. The filtration process is performed by following the steps below:

1. Dissolve 200mg of polyvinlypyrrolidone in 500mL of MilliQ water.
2. If the nanocubes have not been suspended in ethanol, do so at this point by centrifuging the solution at 2900g for 1.5 hours, removing

the supernatant and then suspending the particles in ethanol (200 proof).

3. Take approximately 50mL of the nanocubes in 200-proof ethanol and add them to 150mL of the polyvinylpyrrolidone solution prepared in water.
4. Assemble the vacuum filtration system and then begin the filtration by using the 5µm filter to pass the particles through. Do this step slowly to avoid clogging the filter.
5. After this step pass the particles through the 0.45µm filter, and then follow by passing the particles through the 0.22µm filter. Care should be taken in each step of filtration to not clog the filter papers. This can be assured by not adding all of the particle solution at one time, but instead only adding a small volume of the particles at one time to the filter apparatus. If filtration begins to run very slow, stop the filtration and replace the filter paper. This step is particularly important when using the smaller pore size.
6. The particles can be run through each filter numerous times to narrow the size distribution of the particles. This is particularly important at the final 0.22 µm filter size. At least 3 passes should be attempted with up to 10 at times being necessary. This will result in the loss of some particles but will greatly reduce the size distribution.
7. After filtering the particles, the solution can be divided into 50mL Falcon centrifuge tubes evenly and centrifuged at 2900g for 1.5 hours.
8. The supernatant is removed and the particles are suspended in ethanol (200 proof).

The particles at this point are a very monodisperse, colloidal suspension of silver cubic nanoparticles. The resolution of the various peaks associated with the quadrapolar mode and higher orders of resonance become more distinguishable with repeated filtration passes at the 0.22micron filter step size. Figure 2.1 is a UV-Vis spectrum obtained following the synthesis and purification of the cubic nanoparticles. A scanning electron micrograph of the nanoparticles was obtained and shown in figure 2.2 as well.

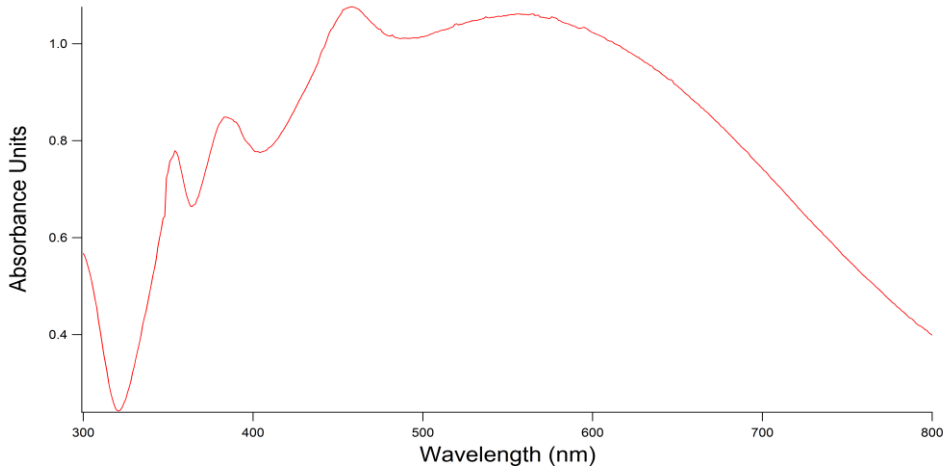

Figure 2.1 - UV-Visible Spectrum of Cubic Silver Nanoparticles. This plot is the UV-Visible spectrum obtained after the synthesis and purification of cubic silver nanoparticles using the polyol synthesis. The solution used as a blank in the UV-Visible spectrum shown here was pure ethanol.

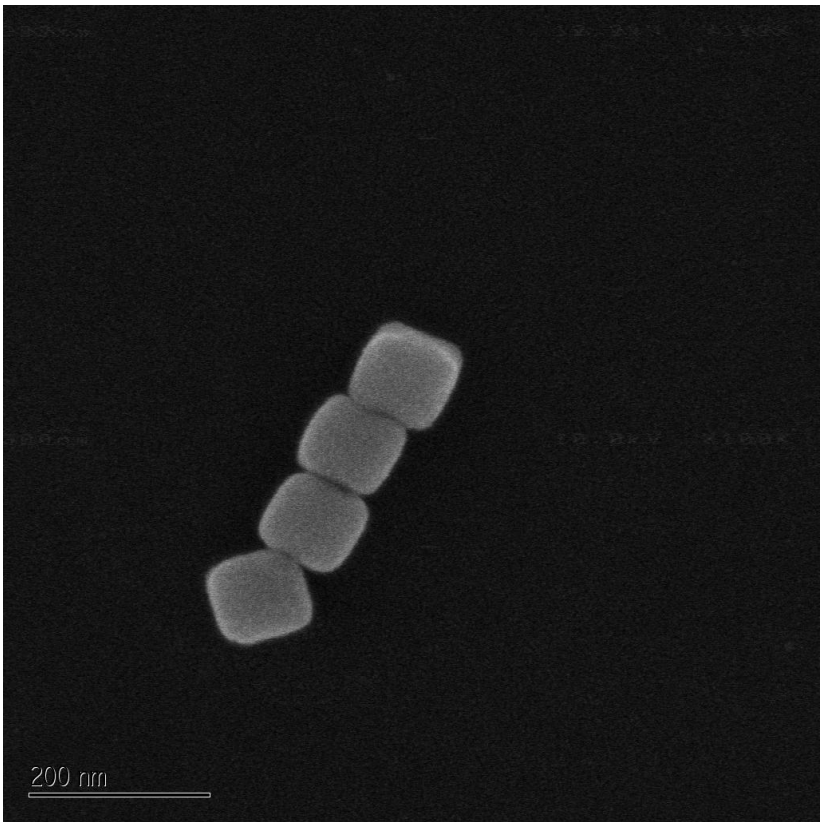

Figure 2.2 - Scanning Electron Micrograph of Cubic Silver Nanoparticles. The silver nanocubes shown here are viewed using a magnification of 100,000.

2.4 Synthesis of Silica Oxide Layer

The polyol synthesis as outlined in section 2.3 produces a very narrow size distribution of silver nanoparticles with a cubic geometry. Using a method, based on the Stöber process, it is possible to produce an ultra thin silica oxide shell surrounding the silver cubic nanoparticles.[3,4] The utility of this silica oxide shell is found not only in the increased stability that the particles show to degradation, but also in the fact that a silica oxide shell renders these particles capable of supporting the formation of a supported lipid bilayer. This modification step to the cubic silver nanoparticles creates a very thin shell of silica oxide with thickness dimensions, measured with Transmission Electron Microscopy to be approximately 4nm (3.91$\pm$ 0.18nm).[3] The radius of curvature of the cubes corners was determined from these TEM micrographs to be 19nm.[3] This is a significant feature as it has been shown that the minimum sized spherical silica particle that supports the formation of a stable supported lipid bilayer has a radius of 19nm.[3] The formation of supported lipid bilayers from single unilaminar vesicles (SUVs) is spontaneous on a number of surfaces including silica surfaces.[3] These silica coated silver nanoparticles ($Ag@SiO_2$) provide a homogenous solution-based nanoparticle assay capable of incorporating the functionalization flexibility and experimental possibilities of the support lipid bilayer system. By incorporating various lipids into the supported lipid bilayer's composition it is possible to create a variety of fluid bilayers surfaces, which can display a number of chemical groups allowing for the tethering of additional molecules of interest to the surface of the supported lipid bilayer. This allows for the modification of the nanoparticles surface to introduce bio-molecules such as antibodies and other molecules that can serve as capture agents as detailed earlier in regards to the construction of the ELISA. There are a large variety of commercially available functionalized lipid molecules that allow for customizable surfaces to be created easily and reproducibly at the particles surface. The formation of the supported lipid bilayer and the control over its composition provides a very versatile platform for developing surfaces that mimic cellular membranes and allows for the interrogation of these surfaces in a controllable manner.

The method for the synthesis of a thin silica shell at the surface of the silver nanoparticle is detailed below. It is assumed that the particles have been stored in ethanol and have been filtered extensively as outlined in section 2.3. The materials for the synthesis include, ammonium hydroxide 28%, ethanol (200 proof), and tetraethyl orthosilicate, which were all purchased from Sigma Aldrich. 50mL Falcon centrifuge tubes were purchased from Fisher Scientific.

1. An aliquot of 1mL of the bare silver nanoparticles suspended in ethanol is added to a 50mL Falcon centrifuge tube.

2. Add 15mL of ethanol (200 proof) to the 1mL of nanocubes.
3. Prepare of solution of 0.28% Ammonium Hydroxide by diluting the 28% Ammonium Hydroxide with 18.2 MΩ·cm deionized (DI) water.
4. Add 3900µL of 18.2 MΩ·cm deionized (DI) water, 600µL of 0.28% Ammonium Hydroxide and 1200µL of tertraethyl orthosilicate to the solution of cubes in ethanol in a 50mL Falcon centrifuge tube.
5. Place the 50mL Falcon tube into a sonicator bath and sonicate for 45 minutes.
6. After 45 minutes, add 10mL of ethanol to the reaction and centrifuge at 7000g for 3 minutes.
7. Remove 10mL of the supernatant.
8. Centrifuge the reaction tube again at 7000g for 3 minutes.
9. Remove 15mL of the supernatant.
10. Add 45mL of ethanol to the reaction tube and centrifuge at 3000g for 25 minutes.
11. Remove the supernatant.
12. Add 45mL of 18.2 MΩ·cm deionized (DI) water to reaction tube and centrifuge for 20 minutes at 3000g.
13. Remove as much supernatant as possible without disturbing the nanoparticle pellet.
14. Centrifuge at 3000g for 10 minutes.
15. Remove remaining supernatant.
16. Add 45mL of 18.2 MΩ·cm deionized (DI) water
17. Repeat the centrifugation at 3000g twice more to thoroughly clean the nanoparticles.
18. After the final centrifuge step, suspend the particles in 1mL of 18MΩ pure water.
19. The UV-Vis solution spectrum can be checked at this point.
20. This solution of $Ag@SiO_2$ particles in water can be stored at 4°C for at least 1 year.

The silica oxide layer produces a small red shift in the LSPR peak of the quadrapolar LSPR mode, relative to that of the bare silver cubes. This is a result of the thin 4-5nm of silica that is now deposited at the surface of the cube. The change in refractive index relative to the bare cube leads to this spectral red shift. The solution spectrum of a batch of $Ag@SiO_2$ cubic nanoparticles is shown below in figure 2.3. Typically the sensitivity of the particle to molecular binding at the surface will also be reduced as the distance that these particles will be from the actual silver surface is now approximately 4-5nm further than for a bare silver cube. This is a result of the shift sensitivity being a function not only of the mass change at the surface of the particles, but also on the distance this molecular absorption layer is from the nanoparticles surface, as seen in equation 1.6. However, this small loss in sensitivity is necessary to prepare a surface that will be compatible with the formation of a supported lipid bilayer. Additionally, a good

SiO_2 coating prevents the oxidation of the underlying silver particle, allowing the particles to have a shelf life >1 year.[3]

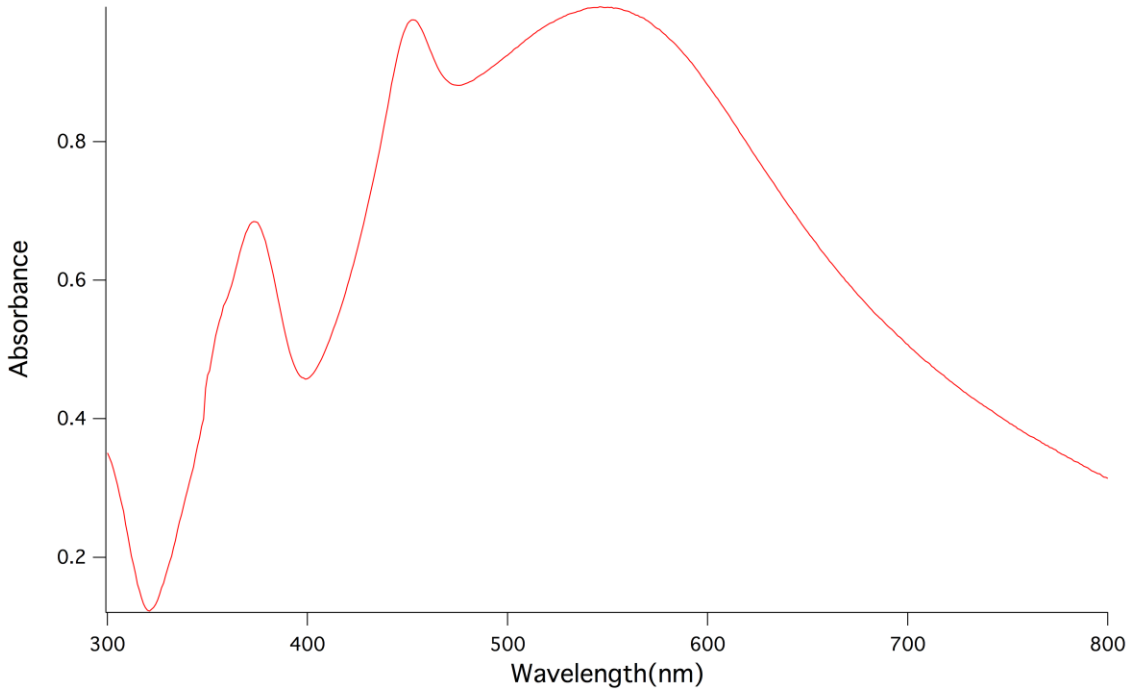

Figure 2.3 - UV-Visible Spectrum for Ag@SiO_2 Nanoparticles. The spectrum is of a colloidal suspension in water of cube shaped Ag@SiO_2 plasmonic nanoparticles. The spectrum was blanked against water.

The first and second order LSPR modes are located approximately at 560nm and 460nm, corresponding to the dipolar and quadrupolar LSPR modes respectively.[1] The maximum value of these peaks were determined by using a polynomial fit.[3] Also worth mentioning here is the width of each of the peaks shown in figure 2.3. The width of the quadrupolar LSPR mode located approximately at 460nm is narrower than the dipolar peak centered approximately at 560nm. The narrow bandwidth makes the quadrapolar peak ideal for monitoring small changes in its maximum wavelength and serves as the

principle resonance mode to be monitored during LSPR binding experiments. As noted in equation 1.7, the figure of merit (FOM), describing the sensitivity of plasmonic nanoparticles resonance frequencies to changes in the refractive index at the interface between the particle and the bulk solution, is defined as the responsiveness of the particles to changes in the refractive index, m, divided by the full width at half maximum of the resonance mode being monitored. The narrow width of the quadrupolar mode, relative to that of the dipolar mode, yields a higher figure of merit for the quadrapolar mode in comparison to that of the dipole mode.

In order to quantify the responsive factor, m, as well as the figure of merit for the $Ag@SiO_2$ nanoparticles, the solution UV-Visible spectrum was obtained for a suspension of particles in an aqueous environment of increasing glycerol percentage to control the refractive index of the medium each particle was exposed to in solution. The results of this calibration show the expected linear shift in the peak absorption wavelength of the quadrapolar peak as a function of the change in the refractive index of the surrounding medium. The LSPR maximum for each glycerol percentage was calculated by, first determining the maximum value of absorbance within the peak associated with the quadrapolar mode, and then finding the corresponding wavelength to this absorbance. This maximum absorbance was interpolated by fitting the UV-Visible spectrum by using a polynomial fit.[3] The LSPR shifts in nanometers were then obtained by comparing the maximum wavelength of the 0% glycerol solution to each of the wavelength maximums obtained in the solutions of increasing glycerol percentage. The results of these LSPR shifts are shown in figure 2.4. The full width at half maximum of the quadrapolar peak is approximately 20nm. The response factor m of these nanoparticles was determined to be $228.43 nm \cdot RIU^{-1}$. Equation 1.7 predicts that the corresponding FOM for this batch of $Ag@SiO_2$ nanoparticles to be 11.4.

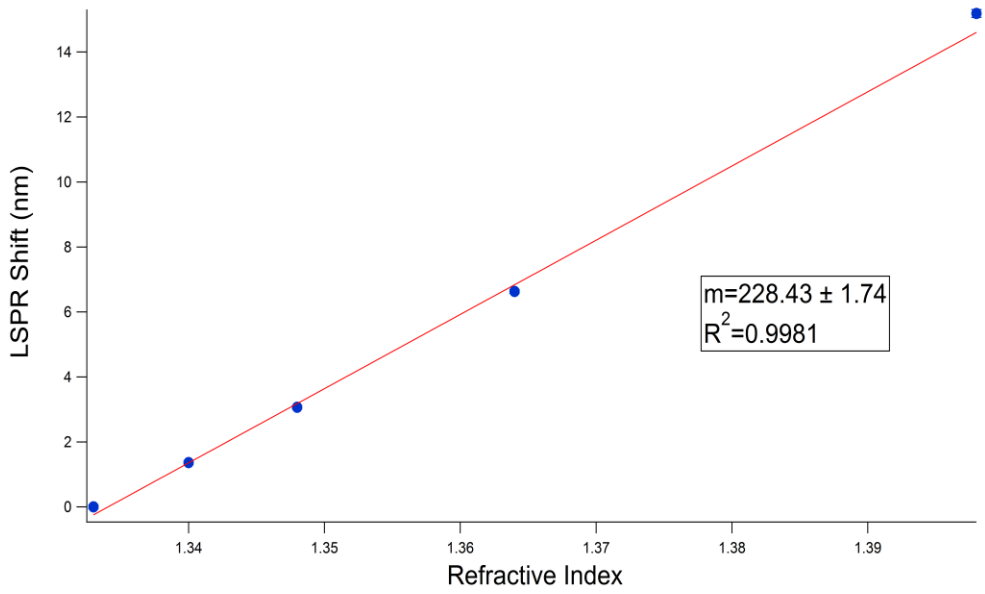

Figure 2.4 – $Ag@SiO_2$ Nanoparticles LSPR Shift Versus Surrounding Medium's Refractive Index - The LSPR Shift as function of the refractive index of the solution of glycerol the particles are suspended. The slope m represents the response factor of the nanoparticles to changes in the refractive index. These particles have a response factor m of 228.43 nm RIU^{-1}, yielding a figure of merit of 11.4.

2.5 - Streptavidin Biotin Titration: Calibration of Nanoparticles

In order to calibrate the nanoparticles LSPR spectral shift sensitivity in terms of the mass absorbed at the surface of the nanoparticle in addition to the previous calibration of the particles response to changes in the bulk refractive index changes of the surrounding medium, a streptavidin biotin binding titration curve was generated on the cubes using UV-Vis spectroscopy. The titration consists of preparing a series of vesicles solutions where the lipid composition is composed of 1,2-dioleoyl-sn-glycero-3-phosphocholine (DOPC) with increasing percentages of 1-oleoyl-2-(12-biotinyl(aminododecanoyl))-*sn*-glycero-3-phosphoethanolamine (Biotin-Cap-PE). These vesicles were used to form a support lipid bilayer on the nanocube particles so that each suspension exhibited an increasing number of biotin molecules at its surface. The various lipid compositions were exposed to a 1uM solution of streptavidin and allowed to come to equilibrium for 3 hours. The biotin binding sites, within the supported lipid bilayer formed on the nanocubes were assumed to be saturated under these conditions, allowing for the calculation of the LSPR shift versus the mass absorbed at the surface. This was performed by using the calculated number of biotin present within each supported lipid bilayer depending on the percentage of Biotin-Cap-PE present in the supported lipid bilayer. The number of Biotin-Cap-

PE was determined using the geometric dimensions of the nanocubes, as well as the footprint of a typical DOPC lipid, which has an area of 0.72nm^2

The following lipids were purchased from Avanti Polar Lipids (Alabaster, AL): 1,2-dioleoyl-sn-glycero-3-phosphocholine (DOPC) and 1,2-dioleoyl-sn-glycero-3-phosphoethanolamine-N-(cap-biotinyl) (Biotinyl-Cap-PE). The UV-Vis transmission spectrophotometer used in these experiments was the Cary 100 (Varian, Inc, Santa Clara, CA). An *Avanti* Mini-Extruder along with membrane supports and 100nm pore size filters were purchased from Avanti Polar Lipids (Alabaster, AL). A bench top centrifuge was purchased from VWR (minicentrifuge, VWR, maximum RCF = 2000g). Bovine Serum Albumin (BSA) and Streptavidin Affinity Purified, lyophilized from 10mM Potassium Phosphate were purchased from Sigma Aldrich. Sub-Micro quartz spectrophotometer cuvettes #16.40-Q-10/Z151 were purchases from Starna Cells Inc. (Atrascadero, CA).

The lipids were prepared by first drying in a 25mL round bottom flask, using a Rotovap. The dried lipids were rehydrated using 0.1M PBS (pH 7.4) and then hand-extruded at a temperature of 42°C. An aliquot of SiO_2@Ag nanoparticles was mixed with each vesicle solution of unique lipid composition at a volume ratio of 1:2 of particles to vesicles and incubated for 20 minutes. The composition of the lipids prepared for this titration varied from 0% to 0.8% Biotinyl-Cap-PE with the amount of DOPC adjusted in each case. After 20 minutes Bovine Serum Albumin was added to the nanoparticle vesicle solution mixture to final concentration of 0.05mg/mL and allowed to block any defects in the supported lipid bilayer for 30 minutes. Following blocking, the mixture was centrifuged using the VWR bench top centrifuge followed by subsequent removal of the supernatant. The cubes were suspended in 0.1M PBS with a pH of 7.4 and diluted to a working concentration of 1pM.

The supported lipid bilayer coated nanoparticles were exposed to a 1µM streptavidin solution and allowed to come to equilibrium for 3 hours. The biotin binding sites should be saturated at these concentrations and allows for the calculation of the number of streptavidin bound to each particle as explained above. The suspensions of cubes were analyzed using the Cary 100 spectrophotometer and the peak LSPR wavelength, $\lambda_{max,}$ was determined by fitting transmission spectra to a seventh-order polynomial.[3] The number of biotin present in each cube was determined using the footprint size of 0.72nm^2 for DOPC lipids. The results of this titration relating the number of streptavidin bound to each cube and its subsequent LSPR shift is shown in figure 2.5

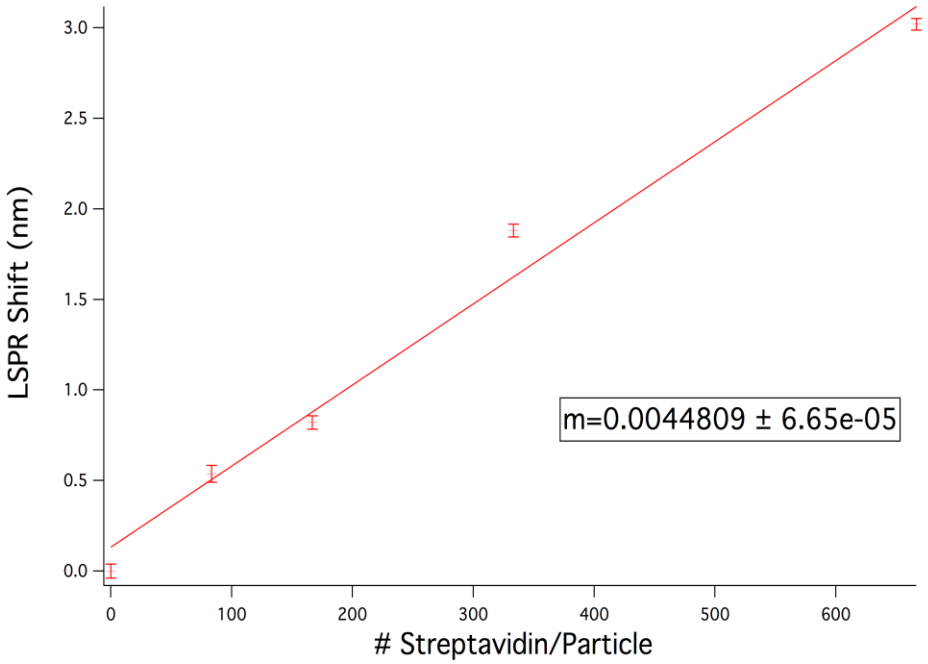

Figure 2.5 – Ag@SiO_2 Nanoparticles LSPR Shift Versus Protein Density. A streptavidin-biotin titration curve showing the LSPR shift versus the number of streptavidin bound to each particle with an increasing percent of biotin in the supported lipid bilayer. The percentage of Biotin-Cap-PE in each supported lipid bilayer used ranged from 0-0.8%. A constant 1µM streptavidin concentration was used at each data point.

2.6 Literature Cited

1. A. R. Tao, P. Sinsermsuksakul, P. Yang, Angew.Chem. 2006, 118, 4713–4717; Angew.Chem. Int. Ed. 2006, 45, 4597.
2. Y. Sun, Y. Xia, Science 2002, 298, 2176.
3. Wu H-J., Henzie J., W-C. Lin, Rhodes C., Li Z., Sartorel E., Thorner J., Yang P., Groves J.T., Nature Methods 2012*,* 9, 1189–1191.
4. Stöber, W., Fink, A. & Bohn, E. *J. Colloid Interface Sci., 1968,* 26, 62–69.

.

Chapter 3

Dark Field Scattering Spectra of Membrane Encapsulated Plasmonic Nanoparticles

Chapter 3.1 Introduction

Dark Field Microscopy is a microscopic technique that utilizes the scattering of light from objects. The basic concept is that light illuminates the object at a high angle of incidence after passing though a high numerical aperture (NA) dark field condenser. The dark field condenser consist of a tube with a small annulus at the end of the tube which blocks light except for a small portion at the outer ring of this annulus. This provides a hollow cone of light that will illuminate the sample at a high angle of incidence, while excluding all other light. The scattered light is then collected by an objective with a numerical aperture lower than that of the dark field condenser assuring that only the scattered light is collected. The first recorded dark field microscope and its application, termed ultramicroscopy at the time, was demonstrated by Zsigmondy and Siedentopf.[1,2] They illuminated a sample at an angle perpendicular to the objective so that only scattered light due to Raleigh scattering was collected. This greatly reduced background noise and increased the signal to noise ratio (s/n).[1] Additional benefits of using dark field scattering microscopy are that objects smaller than the diffraction limit may be visualized by collecting the light scattered from these objects. When using plasmonic nanoparticles this scattered light is extremely intense making plasmonic nanoparticles well suited for imaging using the dark field scattering microscope. The scattering cross section for spherical plasmonic nanoparticles is extremely large relative to their size.[1] The scattering cross-sectional area, for a spherical nanoparticle, can be calculated from equation 3.1.

$$\boldsymbol{\sigma = \frac{3}{2\pi}\left(\frac{\omega}{c}\right)^4 \varepsilon_{diel}^2 V^2 \frac{\left(\varepsilon'_{met}-\varepsilon_{diel}\right)^2+\left(\varepsilon''_{met}\right)^2}{\left(\varepsilon'_{met}+2\varepsilon_{diel}\right)^2+\left(\varepsilon''_{met}\right)^2}} \quad \textbf{(3.1)}$$

In equation 3.1, ε'_{met}, ε''_{met} represent the real and imaginary portion of the metals dielectric constant, respectively, while ε_{diel} represents the dielectric constant of the surrounding medium.[1] V is the volume of the particle, so the scattering cross section scales according to the 6th power of the radius.[1] The scattering cross section of a particle, is maximized at the resonance frequency, which corresponds to situation when the real component of the metals dielectric constant is equal to twice the negative value of the surrounding medium's dielectric constant. This accounts of the color of light scattered by the particles, as this frequency of light will be scattered predominately relative to all other colors of light to which the particles are exposed. The large cross-sectional area of these relatively small nanoparticles allows for the imaging of individual plasmonic nanoparticles, regardless of the fact that they are smaller than the diffraction limit. The scattering spectra of plasmonic nanoparticles, as previously illustrated in chapter 1, exhibit peaks that correspond to the resonant frequencies of the surface electrons oscillations. This scattering of light, due to the resonance of the surface electrons in the nanoparticles, is extremely intense. The absorption and scattering cross-sections of silver and gold nanoparticles are many times their geometric size.[3,4,5] This extremely large scattering cross-sectional area makes plasmonic nanoparticles very well suited for single particle imaging using dark field scattering microscopy. This feature allows the interrogation of single

particles without the averaging implicit in bulk measurements when using ensemble methods such as UV-Visible spectroscopy.

When dark field microscopes are used in conjunction with a spectrophotometer, the scattered light is focused first onto a grating element, followed by the light being directed on to a spectrophotometer's charge-coupled device (CCD) camera where it is recorded. This allows for the collection of the detailed Localized Surface Plasmon Resonance scattering spectra for individual particles. Much like UV-Visible spectroscopy, this will allow for the monitoring of small changes in the peak resonance frequency, due to the change in local refractive index at the interface of the plasmonic nanoparticle and the surrounding medium. This has advantages over UV-Visible spectroscopy. The averaging effects of bulk solutions, where the contributions from an extremely high number of particles are collected, are not seen and small, unique features of individual particles can be resolved. The first spectroscopic studies of single metal particles were reported by the Schultz and Feldmann groups.[6,7,8,9,10]

Experiments involving single particle interrogation do have additional requirements than those in solution using UV-Visible spectroscopy. The most important requirement is that the particle be immobilized onto the underlying substrate. For bare silver nanoparticles, where the spectrum is collected in air, a small aliquot of a colloidal suspension can be deposited onto a bare microscope slide and allowed to dry. This will immobilize the cubes due to electrostatic interactions, however this situation does not allow for the introduction of new solvents, or solutions of ligands such as protein, DNA, or other chemical compounds in solution. If the solution spectrum of individual particles is to be obtained, a method for immobilizing the particles to the substrate is going to be required above that used in the experiments conducted with the particles simply exposed to air. This immobilization will be performed within a flow cell. The use of flow cells allows for the interrogation single particles, while exposing them to various solvents and solutions of differing concentrations of dissolved molecules. This is necessary in order to conduct experiments where a single nanoparticle is observed under various conditions in an aqueous environment. A method for immobilizing the particles to the substrate of a flow cell will be outlined in section 3.2.

3.2 Flow Cell Fabrication

The fabrication of a flow cell compatible with the dark field microscope arrangement requires the following items. Corning EAGLE XG Glass slides 75mm x 25mm x 0.7mm were purchased from MTI Corporation (Richmond, CA), 0.125 x 48.00 x 96.00 CLR Surlyn 8940 Thermoplastic Thermova was purchased from Solaronix (Aubonne, Switzerland), Bovine Serum Albumin (BSA), Streptavidin Affinity Purified, lyophilized from 10mM Potassium Phosphate, Cholera Toxin B subunit ≥95% (SDS-PAGE), lyophilized powder and 0.5mL plastic centrifuge tubes were purchased from Sigma Aldrich, D 263® M – Glass

Microscopy Cover Slips were purchased from Schott North America (San Jose, CA). The following lipids were purchased from Avanti Polar Lipids (Alabaster, AL): 1,2-dioleoyl-sn-glycero-3-phosphocholine (DOPC), 1,2-dioleoyl-sn-glycero-3-phosphoethanolamine-N-(cap-biotinyl) (Biotinyl-Cap-PE). An *Avanti* Mini-Extruder along with membrane supports and 100nm pore size filters were purchased from Avanti Polar Lipids (Alabaster, AL). *Lyso*-Monosialoganglioside GM_1 (NH_4^+salt) was purchased from Matreya LLC (Pleasant Gap, PA) A bench top centrifuge was purchased from VWR (minicentrifuge, VWR, maximum RCF = 2000g). The dark field microscope utilized an Olympus IX71 microscope, coupled to an Acton Research Corporation Microspec 2300i spectrophotometer. The dark field microscope was used in transmission configuration with a condenser numerical aperture of 1.1-1.5 along with a 40X objective lens of numerical aperture of 0.95. Data collection software for the Microspec 2300i was Winspec32.

A flow cell was constructed by drilling holes at either end of the Eagle XG glass slide. The Eagle XG slide was then sealed to the Schott glass cover slips using the thermoplastic Thermova. A small channel measuring, 65mm x 15mm x 0.1mm (LxWxH), for a total volume of 97.5µL was formed by cutting the thermoplastic Thermova before use to seal the cover slip to the Eagle XG slide. A small injection well was formed by attaching a modified centrifuge tube to each end of the slide at the site of the drilled hole using a quick drying epoxy.

3.3 Immobilization of Nanoparticles

The immobilization of the nanoparticles to the glass substrate was accomplished through the formation of a supported lipid bilayer both within the flow cell chamber as well as surrounding the silver cube nanoparticles. A supported lipid bilayer was prepared with a composition of 97% DOPC and 3% Biotin-Cap-PE. This was injected into the flow cell and allowed to form for 45 minutes. A blocking solution of BSA (0.05mg/mL) was then introduced into the cell and allowed to react for 30 minutes. The cell was washed repeatedly using 0.1M PBS, pH 7.4 and then a 0.1µM solution of Streptavidin in 0.1M PBS with a pH of 7.4, of was injected into the flow cell chamber using a micropipette and allowed to react with the biotin sites within the supported lipid bilayer for 30 minutes. The cell was washed repeatedly using 0.1M PBS, pH 7.4 to remove any unbound Streptavidin from the flow cell.

The binding of Cholera Toxin Subunit B to *lyso*-Monosialoganglioside GM_1 was used as model system to demonstrate the ability of the dark field microscope to monitor LSPR shifts in response to molecular binding events to single particles. Two different supported lipid bilayer nanoparticle solutions were prepared by coating the $Ag@SiO_2$ nanoparticles with two different supported bilayer compositions. The first solution of nanoparticles was prepared by forming a supported lipid bilayer with a lipid composition of 92% DOPC, 3% Biotin-Cap-PE, and 5% GM1, while the other nanoparticle solution's supported lipid bilayer composition was 97% DOPC and 3% Biotin-Cap-PE. The latter will serve as a control situation in which no GM1 is present for binding to the Cholera Toxin

Subunit B. The control situation helps verify the specificity of the nanoparticles binding of Cholera Toxin Subunit B is specific for the GM1 receptors. Spectral shifts in the maximum LSPR wavelength will occur only for binding of the Cholera Toxin Subunit B to the GM1 receptor in the supported lipid bilayer. The absence of the GM1 receptor from the bilayers shows very little spectral shift indicating very little non-specific interaction of the nanoparticles to the Cholera Toxin Subunit B in the absence of the GM1 receptor. The supported lipid bilayer coated nanocube particle suspensions were prepared as described previously in section 2.5 for the streptavidin-biotin calibration curve. The two different compositions of supported lipid bilayer coated nanoparticles were injected into two separate flow cells respectively. The injection was performed following the formation of the supported lipid bilayers within the flow cell chambers. The supported lipid bilayer coated nanoparticles were allowed to bind to the streptavidin previously bound to the Biotin-Cap-PE lipids within the supported lipid bilayer of the flow cell chamber for 30 minutes. The cell was then washed repeatedly with 0.1M PBS, of pH 7.4, to remove any unbound nanoparticles. The immobilization was then verified by visually checking using a dark field microscope. The immobilization of the particles to the underlying substrate was confirmed by observing them for 10 greater than 10 minutes prior to collecting the scattering spectra of a particle. Free particles will diffuse in and out of the frame of view, while immobilized particles will remain stationary.

3.4 Single Particle Scattering Measurements Using Membrane Encapsulated Nanoparticles

As explained above, single particle binding assays exhibit many advantages relative to bulk experiments, where we observe the statistical averaging of many particles. Foremost among these is the number of binding sites or particles to the number of molecules in solution. Since we are exploring single particle interactions with the Cholera Toxin Subunit B, very little actual protein is required, depending on the volume of the cell designed. In these experiments a volume of 100µL was used, which was determined by the dimensions of the cell constructed. This volume can be greatly reduced, however, by the use of micro fluidic chambers. The current state of micro fluidics and the possible minimum volumes used in these experiments will be commented on below.

Before interrogating the binding response of single particles to binding molecular binding events at their surface, the dark field spectrum of $Ag@SiO_2$ particles lacking any supported bilayer was collected by depositing 5µL aliquots of a suspension of the particles in ethanol onto clean microscope slides and then allowing the solvent to evaporate. The particles are immobilized onto the glass substrate in this situation due to electrostatic interactions between the particles and the substrate and so there is no further need to immobilize the particles. Figure 3.1 is a color image of an array of nanoparticles collected on a CCD camera attached to one of the microscopes ports using a 400X magnification. Figure 3.2 illustrates the quadrapolar LSPR spectrum for a single, unmodified

$Ag@SiO_2$ particle. The scattering spectra in figure 3.2, was determined by applying equation 3.2 as explained below.

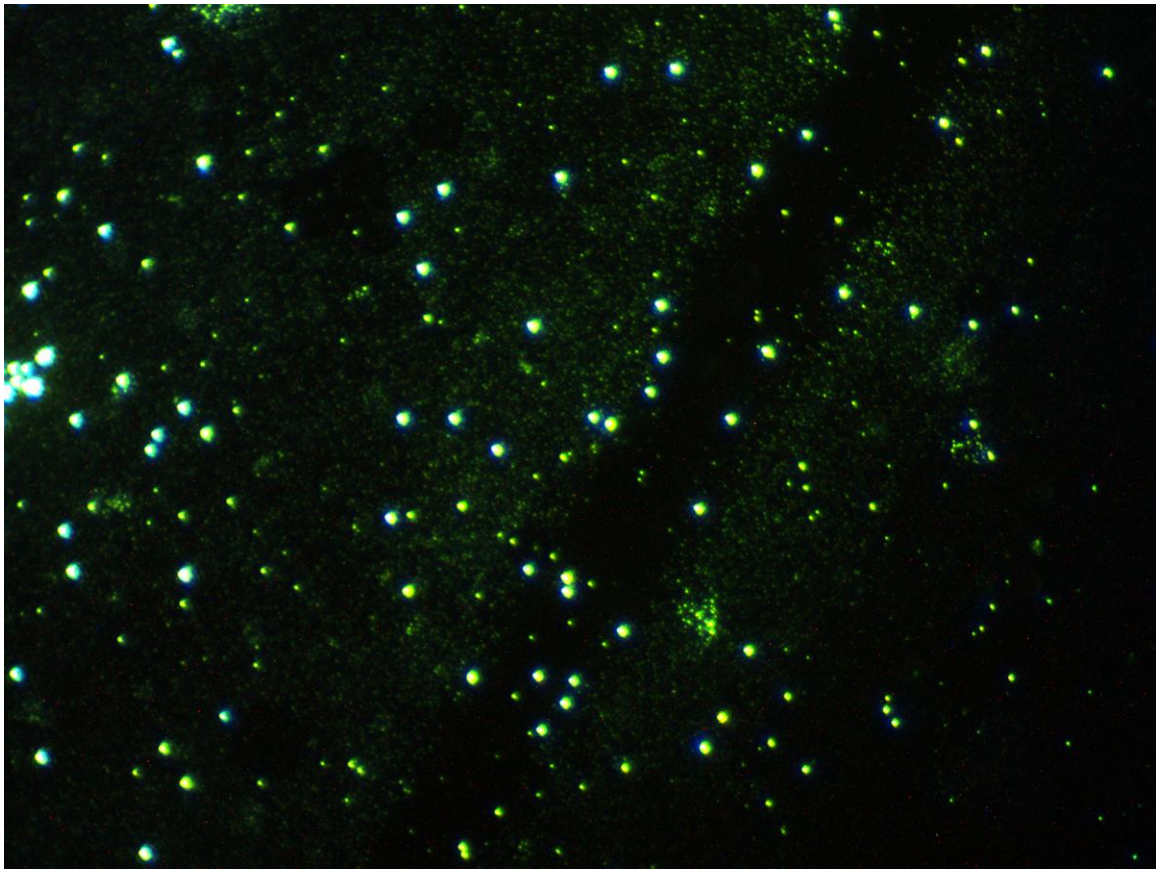

Figure 3.1 – Dark Field Scattering Microscope Color Image of $Ag@SiO_2$ Nanoparticles on a Glass Slide Exposed to Air. The magnification used here is 400X.

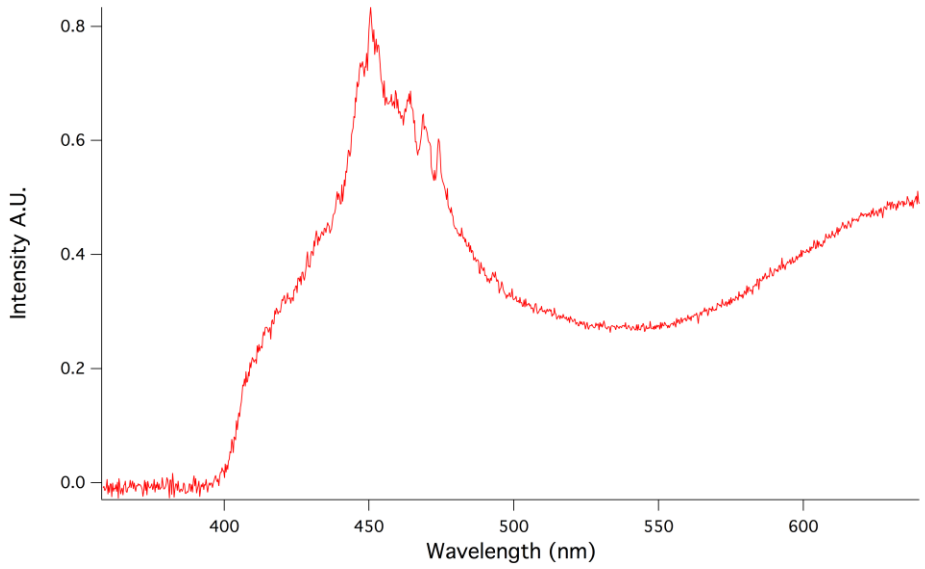

Figure 3.2 – Dark Field Scattering Spectrum of a Single Ag@SiO_2 Nanoparticle in Air. This spectrum indicates that the dominant quadrapolar LSPR peak for this particle is centered approximately at 455nm. The maximum wavelength of the LSPR peak was interpolated by applying a polynomial fit to the scattering spectrum to determine the wavelength of peak intensity.[14]

When analyzing single particles using dark field microscopy, individual particles can be isolated by utilization of two features of the dark field microscope and the associated spectrophotometers software suite. The first is a physical slit between the microscope and the spectrometer, which has micrometer precision and allows for isolation of a narrow region of the field of view within the flow cell. The second is a feature of the Winspec32 software, which allows for the interrogation of specific regions of interest on the CCD camera. These features when used in conjunction, allow for the isolation of individual particles in both x and y-axis of the camera. Images of the field of view when utilizing the spectrophotometer with the micrometer isolation slit both open and closed, are shown in figure 3.3. The top image is with the micrometer slit open while the bottom image is with this slit closed with a width of 4µm.

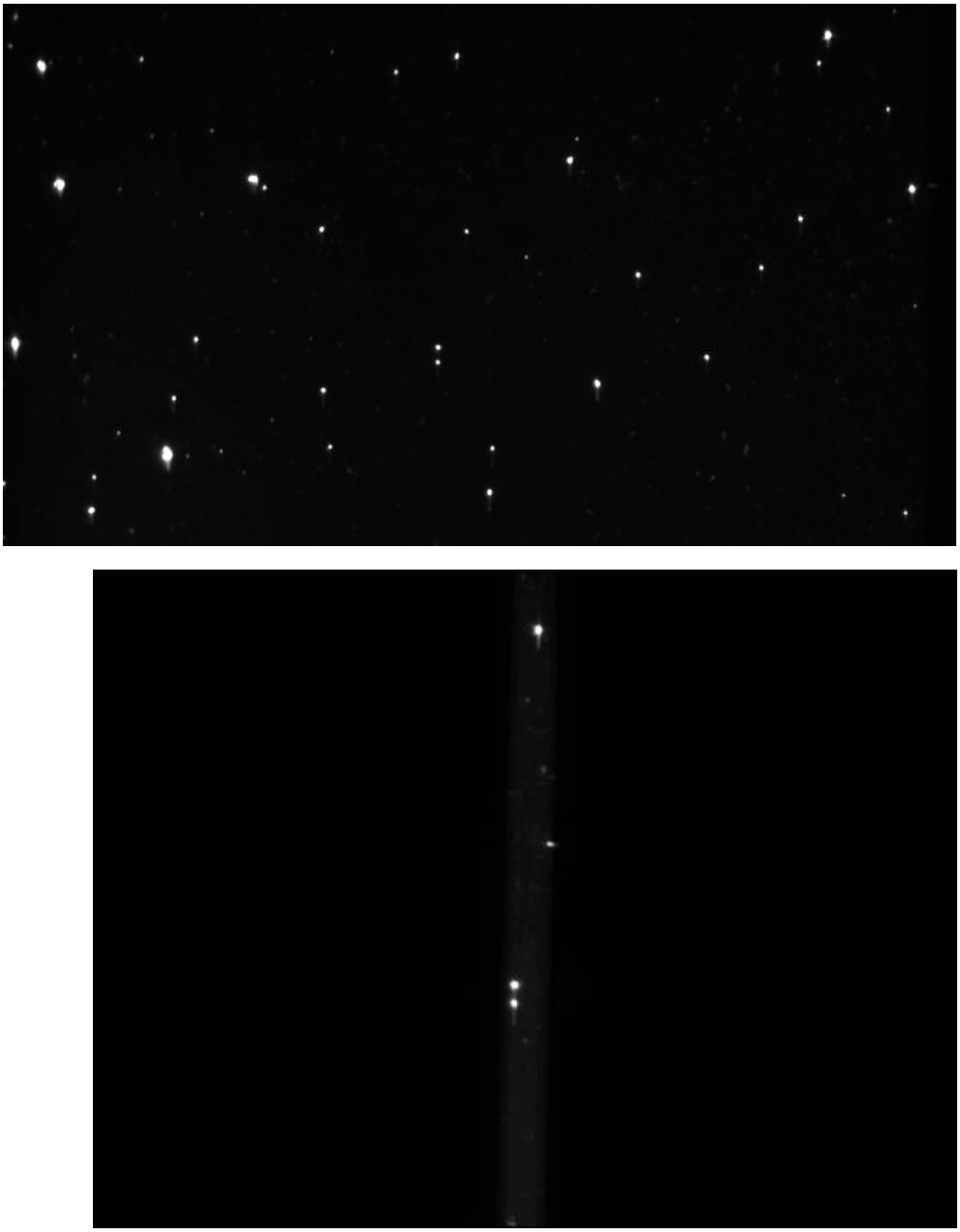

Figure 3.3 – Dark Field Scattering Microscope's Spectrophotometer Field of View. The top image is with the isolation slit disengaged, while the bottom image has the slit engaged to a width of 4µm. This allows for the isolation of individual particles when used with the region of interest software feature in the Winspec32 software of the spectrophotometer.

The spectrum of individual particles was calculated from the data collected by the taking the difference of the intensity spectrum between one isolated particle and the background of the flow cells, where no particles are located. The spectrum intensity was normalized by dividing this adjusted intensity by the intensity of the halogen lamp used to illuminate the sample minus any dark field current present. This is shown in equation 3.2.

$$\boldsymbol{Corrected\ Spectrum} = \frac{[\boldsymbol{Intensity_{Particle} - Intensity_{Background}}]}{[\boldsymbol{Intensity_{Lamp} - Intensity_{DarkCurrent}}]} \quad \textbf{(3.2)}$$

The binding of Cholera Toxin Subunit B to the ganglioside GM1 was used as a demonstration of the potential ability to detect molecular binding events, using single particle dark field scattering experiments. Cholera Toxin is a member of the AB_5 cytotoxin class. Here we used the subunit B_5, which is pentameric in structure. The ganglioside GM1 is also pentameric and is presented on the cell membrane of cells.[11] The supported lipid bilayer surrounding the nanoparticles, mimics a cell membrane presenting the GM1 binding receptor for Cholera Toxin Subunit B. The K_d for Cholera Toxin binding to the GM1 receptor has been reported to be 4.55pM as measured by SPR.[12] In this set of experiments it is important to note that the equilibrium dissociation constant for the Cholera Toxin GM1 system is not the goal of this set of experiments and is not being determined. It has been shown that the supported lipid bilayers composition of GM1 can have a significant influence on the apparent K_d measured.[13] The focus of this experiment instead is to maximize the capturing capacity of the nanoparticles by having a high number of GM1 receptors present on the surface of the particles. A constant 5% GM1 lipid composition in the prepared supported bilayers was utilized as discussed in the materials and methods section for creating the flow cell and supported lipid bilayer coated nanoparticles.

The maximum of the LSPR peak, λ_{max}, was interpolated using a seventh-order polynomial algorithm, which was written in MatLAB.[14] In order to verify that the binding results were indeed specifically a result of the Cholera Toxin Subunit B binding to the GM1 receptors, located within the supported lipid bilayer two different control approaches were utilized. The first control involved the exposure of a solution of Cholera Toxin Subunit B to nanoparticles coated with a supported lipid bilayer, which lacked the GM1 receptor. The second control experiment involved the exposure of the supported lipid bilayer coated nanoparticles, which contained the GM1 receptor, to a solution of BSA in 0.1M PBS, pH- 7.4 and at a concentration 0.1mg-mL^{-1}. Both of these control situations verified that very little non-specific binding occurs in either situation. This was verified for a number of

separate particles in different flow cells. The results of both of these control situations are shown in figures 3.4 and 3.5.

A

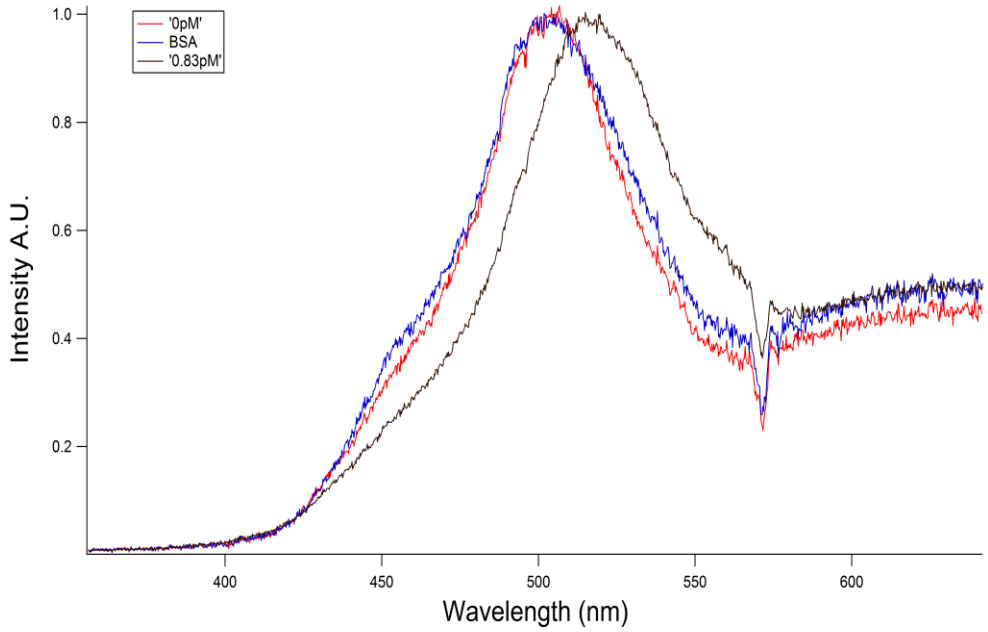

B

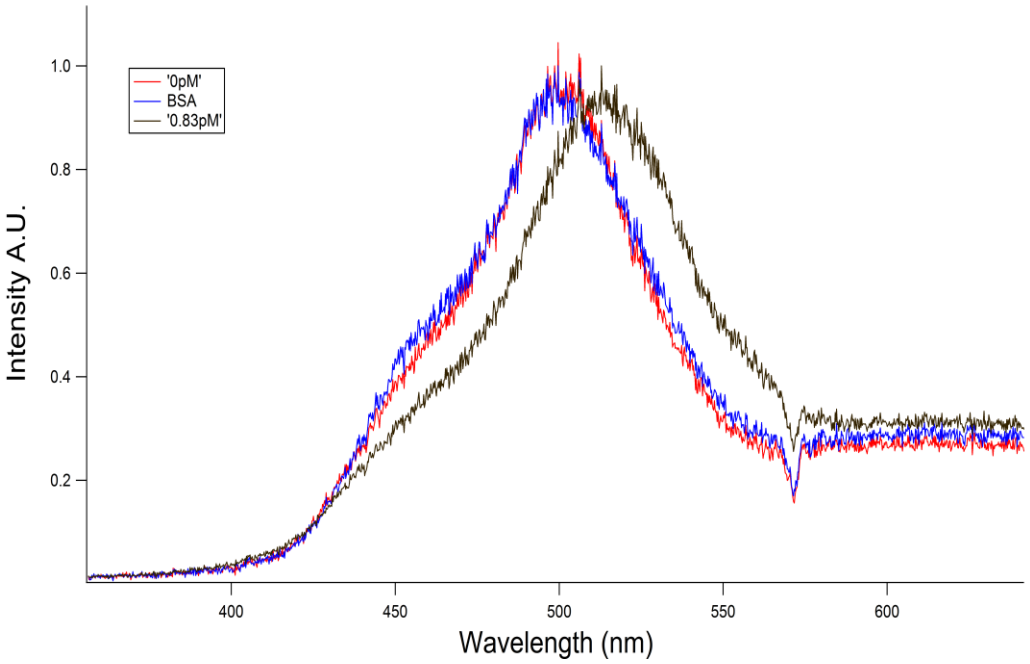

Figure 3.4 – Bovine Serum Albumin Binding Control – Dark Field Scattering Spectrum. A and B are two different single nanoparticles displaying GM1 that were exposed to BSA at a concentration of 0.1mg/mL, followed by Cholera Toxin Subunit B at a concentrations of 0pM and 0.83pM. Very little change in the λ_{max} is observed in BSA exposure relative to the 0pM Cholera Toxin Subunit B.

A

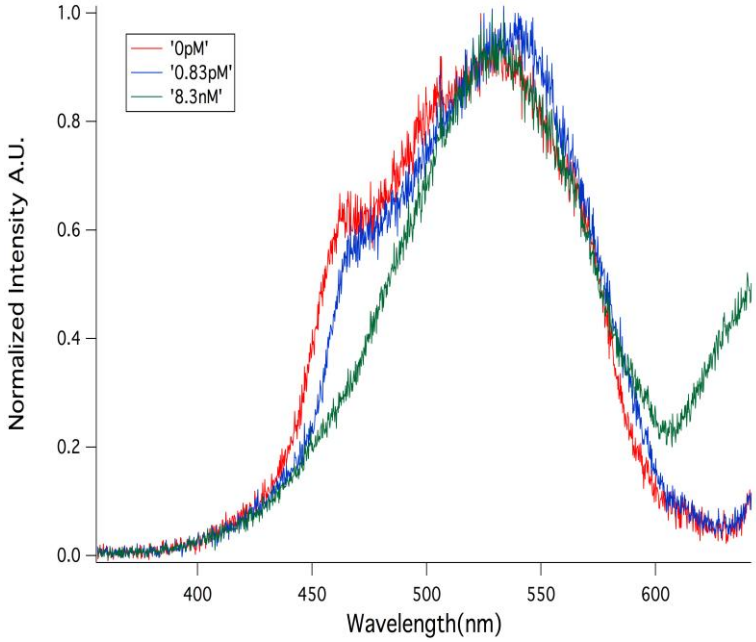

B

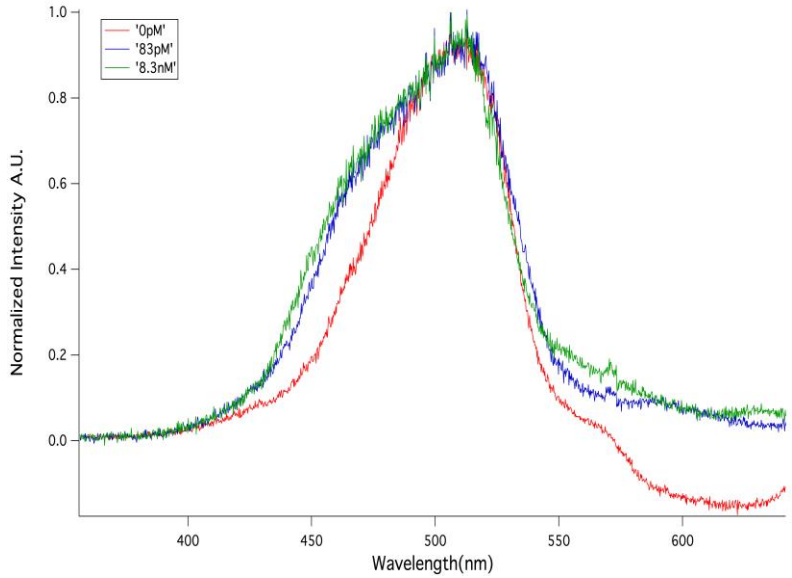

Figure 3.5 - DOPC Bilayer Cholera Toxin Subunit B Binding Control - Dark Field Scattering Spectrum. Graphs A and B above, are the scattering spectra of two different, individual nanoparticles coated with a bilayer lacking GM1 when exposed to solutions of Cholera Toxin Subunit B of concentrations ranging from 0pM to 8.3nM. Both particles, when lacking the GM1 receptor, show very little affinity for the Cholera Toxin Subunit B as indicated by the nearly identical values of the maximum wavelength of scattered light in their LSPR spectra.

The control conditions illustrate that the binding of the cholera toxin to the nanoparticles lacking the receptor GM1 is very minimal. These results suggest that the interaction of the Cholera Toxin Subunit B with the nanoparticles is very specific for only the GM1 receptor within the supported lipid bilayer and not a result of any interaction with the nanoparticle itself. They also demonstrate that proteins other than Cholera Toxin Subunit B show very little binding to the nanoparticles when GM1 is present in the bilayer. Bovine Serum Albumin is used as an example of the interaction of a protein, other than Cholera Toxin Subunit B, with the GM1 receptor on the nanoparticles surface. The LSPR shift for nanoparticles with supported lipid bilayers containing the GM1 receptor, exposed to BSA is less than 0.5nm for graph A and B in figure 3.4. The LSPR shift for the same particle when exposed to 0.83pM of Cholera Toxin Subunit B is 10.2nm. The second control situation, shown in figure 3.5, indicates that the LSPR shift in the maximum wavelength for the LSPR spectra of nanoparticles whose supported lipid bilayers lack the GM1 receptor is less than 0.5nm as well when exposed to Cholera Toxin Subunit B. Both of these LSPR shifts were below the minimum detectable LSPR shift as defined below using equation 3.3. The specificity of the dark field microscope scattering experiment and its ability to detect LSPR shifts above the minimum detectable LSPR shift only for the binding of the Cholera Toxin Subunit B to the GM1 receptor is a significant issue to demonstrate. If LSPR shifts above the minimum detectable shift occur in either of the control scenarios presented in figure 3.4 or 3.5, the specificity of the assay for detecting the binding of the molecule of interest to the receptors present on the particles, is not a valid assumption. The specificity of the particles to bind only to the protein or molecule of interest is a critical factor in both qualitative and quantitative assays. Non-specific interactions at the surface of the particle must be minimized in order to develop a capture assay that is capable of selectively binding only the molecule of interest. The use of the supported lipid bilayer coated nanoparticles platform demonstrates this requirement for the Cholera Toxin Subunit B binding to the GM1 receptor.

The maximum wavelength of scattered light and the shape of each curve in the binding experiments shown in figure 3.5 are of particular note. First a red shift of the maximum wavelength of the LSPR peak is apparent in nearly all particles relative to the bulk solution spectrum shown in figure 2.3. This is accounted for by the interaction of one face of the nanocube with the supported lipid bilayers surrounding the nanoparticle as well the underlying silica substrate. The red shift due to nanoparticles immobilized onto a solid substrate's surface has been experimentally and theoretically shown to occur when nanoparticles are placed in close proximity to materials with different refractive indexes relative to that of the surrounding medium.[15] The effect is dependent on the surface area of the particle, which interacts with the underlying solid substrate.[15] Nanoparticles with a cubic geometry will exhibit a larger red shift in the maximum wavelength of the LSPR peak in comparison to spherical particles, due the larger surface area of the cubic nanoparticle that will interact with the underlying substrate. In addition to the initial red shift of the maximum wavelength in the LSPR peak of the quadrapolar mode, there also appears to be the presence of an additional

small shoulder in the spectrum. This appears centered around approximately around the 450nm region. We attribute these peaks presence to the interaction of the particle with the underlying substrate as well. Van Duyne et al. have shown that the appearance of this blue shifted peak relative to the LSPR quadrapolar peak will appear as a particle approaches a substrate surface with a different refractive index than the bulk medium otherwise surrounding the particle.[15]

Following the control experiments, the scattering spectra of the binding of Cholera Toxin Subunit B to nanoparticles displaying the GM1 receptor were collected. The LSPR shifts of the maximum LSPR wavelength using the UV-Visible spectrometer based assay were collected as well in order to provide a comparison of the bulk solution assay to that of the single particle binding experiments performed using the dark field scattering microscope. The dark field scattering spectra of the binding of Cholera Toxin Subunit B to GM1 receptors on a single nanoparticle is shown in figure 3.6. The calculated LSPR shifts for the maximum wavelength of light scatted relative to the 0pM sample in figure 3.6 is shown in figure 3.7. The y-axis in figure 3.7 represents the LSPR shift of each samples maximum wavelength in the samples LSPR spectrum when compared to the maximum wavelength of the LSPR spectrum for sample containing 0pM of Cholera Toxin Subunit B. The x-axis of figure 3.7 shows the concentrations of Cholera Toxin Subunit B the particle was exposed to and ranges from 0pM to 83pM.

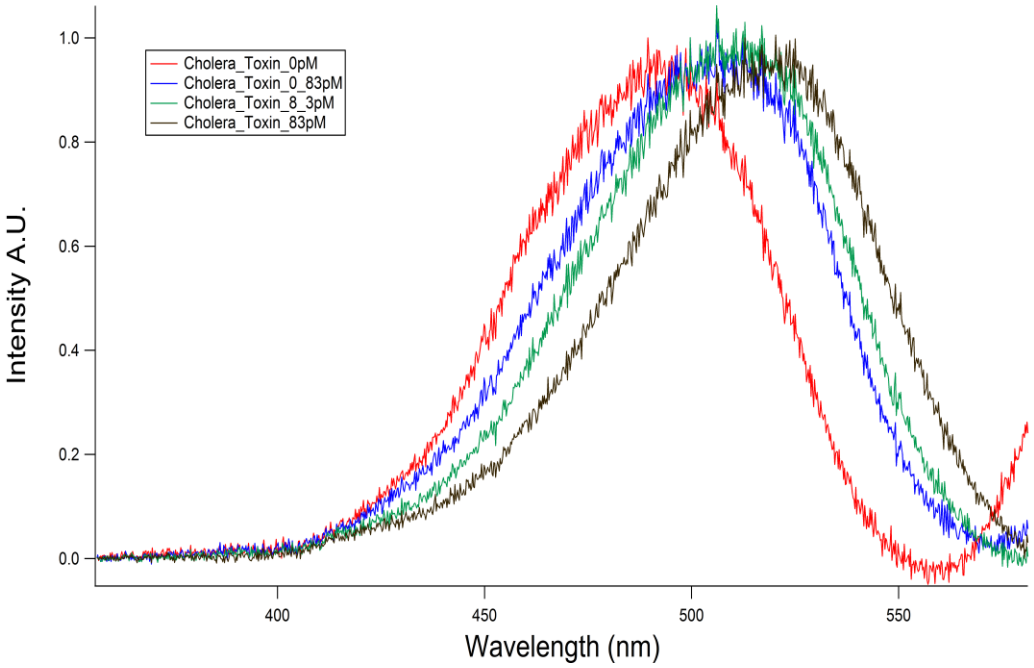

Figure 3.6 – Dark Field Scattering Spectra for a Single Particle Cholera Toxin Subunit B - GM1 Receptor Binding. Single nanoparticle dark field scattering spectrum binding curves showing the LSPR shift in the maximum wavelength of light scattered by the particle as the single particle, displaying the GM1 receptor, is exposed to increasing concentrations of Cholera Toxin Subunit B.

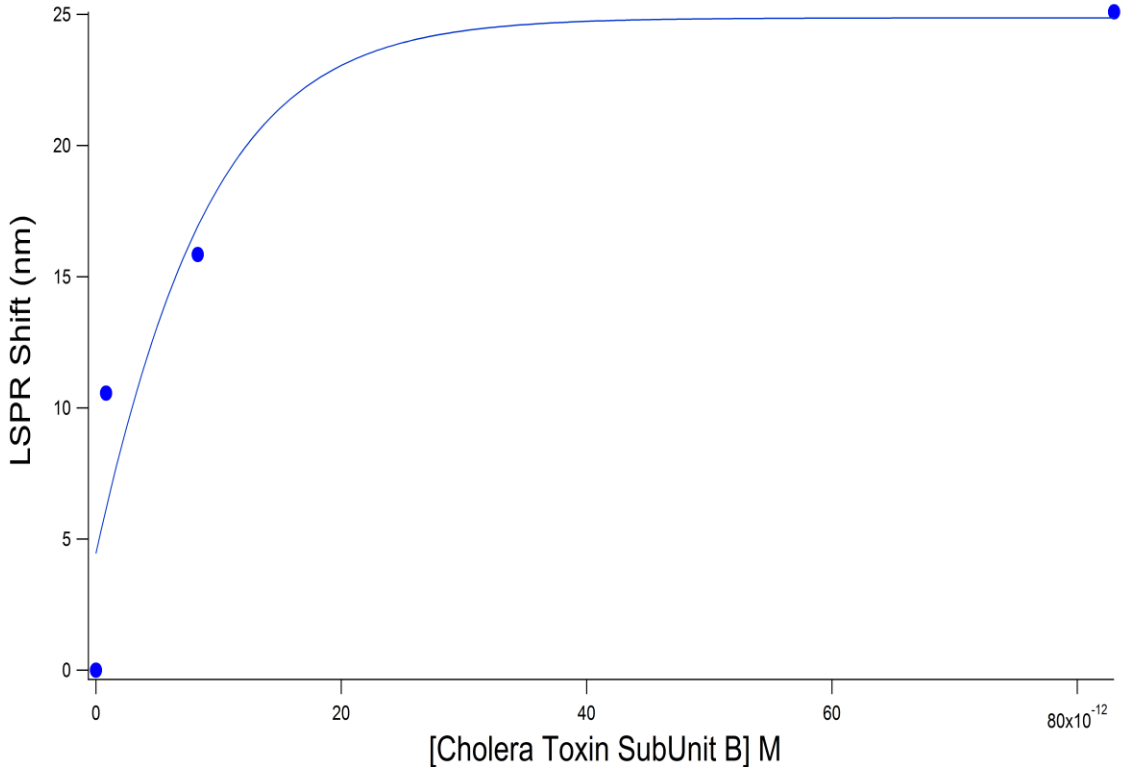

Figure 3.7 - LSPR Shifts for Single Particle Dark Field Scattering Data of Cholera Toxin Subunit B – GM1 Binding. LSPR Shifts for a single particle's dark field scattering spectrums from Figure 3.6 have been calculated and plotted against the Cholera Toxin Subunit B concentrations. A LSPR shift of 10.8nm occurs at a 0.83pM concentration of Cholera Toxin Sub Unit B.

The single particle dark field scattering spectra for an individual particle, which has been exposed to increasing concentrations of Cholera Toxin Subunit B, shows that even at concentrations of Cholera Toxin Subunit B as low as 0.83pM there is an LSPR shift in the maximum wavelength of scattered light from the particle of 10.8nm. The response of the two control situations above showed LSPR shifts below 0.5nm. The LSPR shift is related to the mass of the Cholera Toxin Subunit B bound to the surface of the particle. The LSPR shifts shown in figure 3.7 are significant when compared the magnitude of the LSPR shifts for both the control situations discussed above. Based on the data collected here, the dark field scattering microscope, when utilizing single nanoparticles coated with a supported lipid bilayer with a lipid composition of 5% GM1, are capable of detecting 0.83pM of Cholera Toxin Subunit B in solution. Concentrations below this range were not explored, but based on the large LSPR shift recorded and the minimum LSPR shift detectable using the dark field scattering microscope, it is very likely that the minimum concentration detectable is well below 0.83pM. The minimum detectable LSPR shift using the dark field scattering microscope arrangement in these experiments will be discussed below using equation 3.3, but is of the order of 0.92nm.

In addition to the dark field single particle experiments on Cholera Toxin Subunit B binding the GM1 receptor, a separate solution-based binding experiment was performed using UV-Vis spectroscopic measurements. The preparation of the solution-based particles was identical to that of the dark field experiment, except there was no immobilization of the particles to any underlying glass substrate. The particles were analyzed in solution using a 40µL micro-volume spectrophotometer cell. The nanoparticle solutions were analyzed using a Cary 100 UV-Vis spectrophotometer. The results for the UV-Visible Cholera Toxin Subunit B – GM1 binding experiment are displayed in figure 3.8 and 3.9. Figure 3.8 uses a range of Cholera Toxin Subunit B of 0 to 83µM, while figure 3.9 shows a range of Cholera Toxin Subunit B of 0 to 830nM.

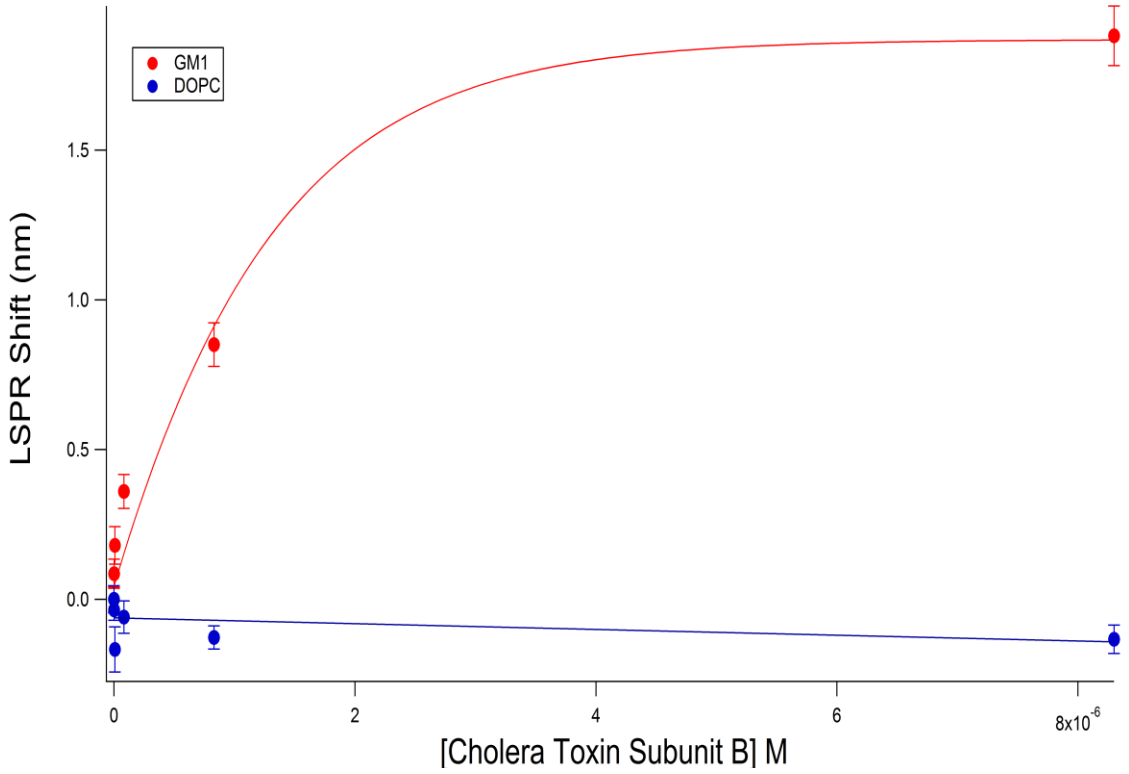

Figure 3.8 – Cholera Toxin Subunit B - GM1 LSPR Shifts for a High Concentration Range of Cholera Toxin Subunit B. The above plots are the LSPR shifts of the UV-Visible spectrometric measurements on nanoparticles coated with supported lipid bilayers both with and without GM1 receptors present in the supported lipid bilayer. The samples lacking the GM1 receptor show very little non-specific binding to the Cholera Toxin Subunit B.

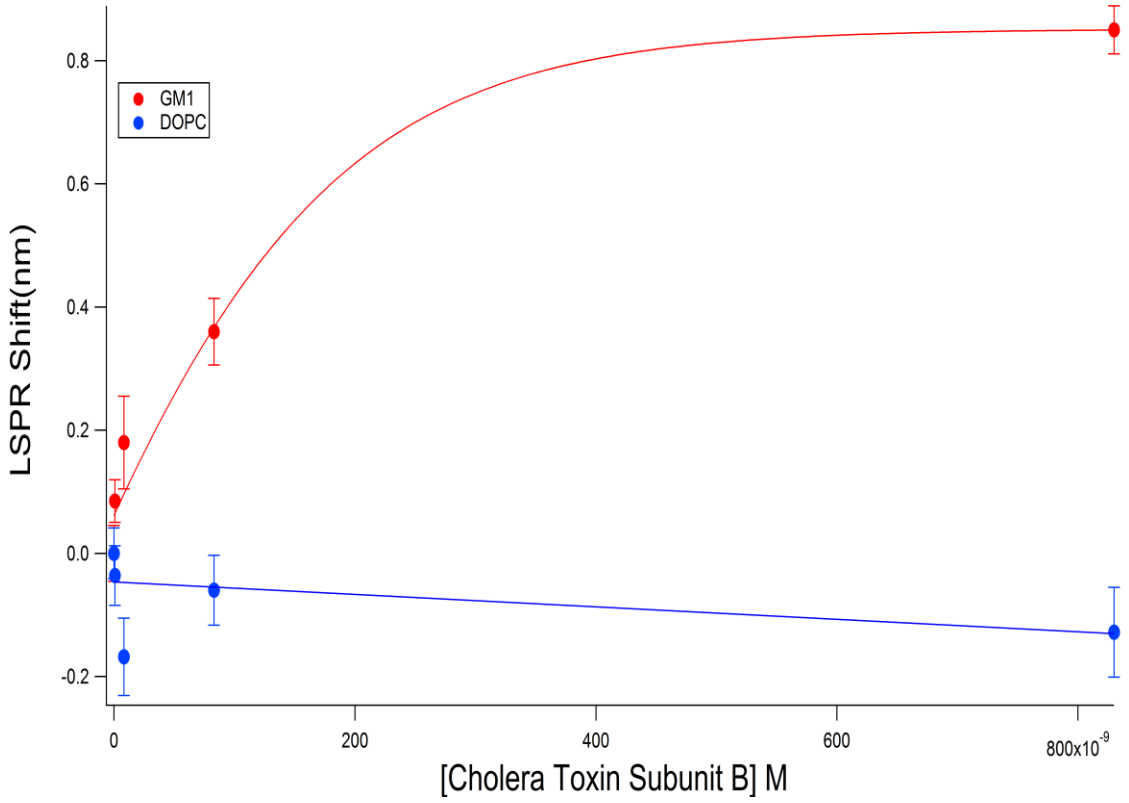

Figure 3.9 – Cholera Toxin Subunit B - GM1 LSPR Shifts for a Low Concentration Range of Cholera Toxin Subunit B. This graph illustrates the LSPR shifts from the UV-Visible spectroscopic measurements on the binding of Cholera Toxin Subunit B to GM1 using a concentration range of 0nM to 830nM. The minimum concentration of Cholera Toxin Subunit B, which elicited a LSPR spectral shift above the reference of 0nM, was 0.83nM.

The UV-Visible and dark field scattering experiments yield drastically different minimum concentrations of Cholera Toxin Subunit B that show detectable LSPR shifts, despite the identical preparation. The dark field scattering experiments were able to detect binding at concentrations of 0.83pM of Cholera Toxin Subunit B, which corresponded to an LSPR shift of 10.8nm. The UV-Visible measurements showed very little LSPR shift due to Cholera Toxin Subunit B binding to the GM1 receptor, until a concentration of 0.83nM Cholera Toxin Subunit B was introduced. This represents a thousand-fold concentration difference between the two experiments. The minimum concentration of Cholera Toxin Subunit B detectable for the UV-Visible should to be between 0.83nM and 0.083nm. The LSPR shift for the 0.83nM Cholera Toxin Subunit B sample was 0.85nm, while the 0.083nm Cholera Toxin Subunit B sample showed less than a 0.01nm LSPR shift. The smallest detectable change in the LSPR shift by our current UV-Visible spectroscope instrument is 0.01nm.[14]

As mentioned above the minimum detectable signal for the LSPR shift in the dark field scattering experiments needs to be determined. The minimum change in the LSPR maximum wavelength that can be detected was calculated by using equation 3.3. This relates the minimum detectable LSPR shift, which can be detected above deviations due to noise in the measurements. It is related to some multiple value of the noise associated with each measurement. The value of **k** will be set to be 3 to establish a minimum detectable LSPR shift that is three times above the standard error obtained from 10 consecutive measurements on a single particle's peak LSPR wavelength.[16]

$$\mathbf{S_m = \bar{S}_{bl} + k s_{bl}} \qquad \textbf{(3.3)}$$

The value of s_{bl} multiplied by k will represent the minimum LSPR shift that is detectable in each experiment. The standard error in the LSPR maximum wavelength obtained from 10 consecutive scattering spectra on one nanoparticle was found to be 0.92nm. This represents the minimum LSPR spectral shift that is a detectable change above that of the variation in the noise of a sample. While the UV-Visible S_m was previously stated to be 0.01nm, which is considerably lower than that of the dark field microscope, the enhancement of the dark field sensitivity to the changes in the refractive index local to the nanoparticles compensates for this fact. As can be seen when comparing figure 3.7 to 3.9 the magnitude of the shifts are quite different. A Cholera Toxin Subunit B concentration of 0.83pM in the dark field scattering spectrum produced an LSPR

shift of 10.56nm. The UV-Visible experiments, at a Cholera Toxin Subunit B concentration of 0.83nM, produced an LSPR shift 0.085nm, which is a factor of 1000 times higher in the Cholera Toxin Subunit B concentration and showing significantly lower LSPR shift associated with this Cholera Toxin Subunit B concentration.

As mentioned previously the small number of molecules required to conduct detection assays, affinity measurements and binding curves when utilizing single particles, compared to solution based assays is one major advantage of the single particle design. This experiment did not seek to optimize this condition, but it is noted that the design of a proper flow cell using micro fluidics can exploit this advantage to a very high degree. For example micro fluidic chambers constructed with inner flow cell dimensions on the order of 1µm x 1µm x 1µm would allow the interrogation, in theory, of 1 single nanocube possessing a diameter of 100nm. The area of the bottom side of this chamber would allow less than 100 nanocubes to be immobilized to the underlying glass substrate. The actually number of molecules of Cholera Toxin Subunit B present in this microscopic volume of 1nL at a concentration of 0.83pM, would be approximately 748 molecules. While this is a theoretical treatment it illustrates that the use of single particle experiments can vastly decrease the amount of ligand necessary when running experiments in vanishingly small volumes and utilizing single nanoparticles.

3.5 Literature Cited

1. Sannomiya T., Junesch J. and Prayanka Rajendran P. Optical Imaging: Technology, Methods and Applications, Imaging, Spectroscopy and Sensing with Single and Coupled Metallic Nanoparticles, 2012, Chapter 1.
2. Zsigmondy R.; Alexander, J. (1909) Colloids and the ultramicroscope; a manual of colloid chemistry and ultramicroscopy, New York, John Wiley & Sons.
3. Hu M., Novo C., Funston A., Wan H., Staleva H., Zou S., Mulvaney P., Xiae Y., and Hartland G.V., Journal of Material Chemistry, 2008, 18, 1949–1960 | 1949
4. Van de Hulst H.C., Light Scattering by Small Particles, Dover Publications, New York, 1981.
5. Zuloaga, J.; Prodan, E.; Nordlander, P. (2009) Nano Lett. 9, 887-891.
6. Knight, M. W.; Wu, Y.; Lassiter, J. B.; Nordlander, P.; Halas, N. J. (2009) Nano Lett. 9, 2188-2192.
7. Sonnichsen C., Geier S., Hecker N.E., Von Plessen G., Feldmann J., H. Ditlbacher , B. Lamprecht, J. R. Krenn, F. R. Aussenegg, V. Z. H. Chan, J. P. Spatz and M. Moller, Appl. Phys. Lett., 2000, 77, 2949.
8. Schultz S., Smith D.R., Mock J.J., and Schultz D.A., Proc. Natl. Acad. Sci. U. S. A., 2000, 97, 996.
9. Sonnichsen C., Franzl T., Wilk T., Von Plessen G., Feldmann J., Wilson O., and Mulvaney P., Phys. Rev. Lett., 2002, 88, 077402.
10. Mock J., Barbic M., Smith D.R., Schultz D.A., and Schultz S, J. Chem. Phys., 2002, 116, 6755.
11. Murray, W. A.; Barnes, W. L. (2007) Adv. Mater. 19, 3771-3782.
12. Kuziemko G.M., Stroh M., and Stevens R.C., Biochemistry, 1996, Vol. 35, No. 20.
13. Shi J., Yang T., Kataoka S., Zhang Y., Diaz A.J., and Cremer P.S., Journal of American Chemical Society, 2007 129(18): 5954–5961.
14. Wu H-J., Henzie J., W-C. Lin, Rhodes C., Li Z., Sartorel E., Thorner J., Yang P., Groves J.T., Nature Methods 2012, 9, 1189–1191.
15. Sherry L.J., Chang S-H., Wiley B.J., Xia Y., Schatz G.C., and Van Duyne R.P., Nano Lett., 2005, 5, 2034-2038.
16. Skoog D.A., Holler F.J., Nieman T.A., (1998) *Principles of Instrumental Analysis, 5th Edition.* Orlando, FL:Saunders Publication Company.

Chapter 4

Backscattering Interferometry Measurements on Membrane Encapsulated Plasmonic Nanoparticles

4.1 Introduction

Backscattering interferometry is a versatile technique with an exquisite sensitivity to small changes in refractive index. Interferometry is one of the most sensitive optical interrogation methods known and has been used to screen molecular interactions in surface binding modes.[1] The physical mechanism of back scattering interferometry (BSI) is based on an interference pattern generated between an incident light beam and a back scattered beam of light after it passes through a sample. Interference patters are generated based on the differences in the phases of the two light beams. For example if both light beams are completely in phase there would be a complete constructive interference pattern generated, whereas if both light beams were completely out of phase there would be complete destructive interference and loss of the light wave pattern. In practical measurements what we see is that the incident light beam when passing through the medium to be interrogated will undergo a phase change related to the differences in the refractive index of the two medium's that the beam of light moves between. In most situations this will be the difference between the refractive index of air and the refractive index of the aqueous solution being interrogated, although this is not a requirement, it is the most common experimental arrangement. The difference in refractive indexes between the air and the liquid media the light travels thru will change the actual path length of the two light beams. This difference in path length leads to a change in the phase of the light beams relative to one another. The different phases of the light waves will interact to produce an interference fringe pattern as a result of constructive and destructive interference. This interference pattern can be projected onto a detector such as a CCD camera allowing for monitoring of changes in this interference pattern due to changes in the phase of each wave as the refractive index of one of the mediums changes. The changes in the refractive index of one of the medium's can be a result of increasing the concentration of dissolved molecules, binding events between two molecules in solution, or even changes in the conformational shape of molecules such as proteins. Modeling of the physical mechanism behind the BSI optical phenomenon indicates that a multi-pass configuration leads to a long effective path-length and high sensitivity.[1] The interference between the two light beams, will produce a fringe pattern which can be projected onto the 2-dimensional CCD camera pixel array. Bornhop et al. have shown that the ability of BSI to detect minute changes in refractive indexes can be measured with a resolution of limit of $\Delta RI = 10^{-6}$.[1] This change in refractive index can be the result of a number of physical changes including the absorption of mass at a surface, the change in refractive index of a bulk solution as well as conformational changes in complex molecules.[1] A illustration of a general interference pattern is shown in figure 4.1. While this is not illustrative of the backscattering interferometry experimental

arrangement, it does demonstrate the phenomenon of interference between two light waves of differing phase and the corresponding interference pattern generated as result of the difference in phase between the two interacting beams of light due to differences in the path length each beam travels. In the BSI the path length difference between these two beams of light will be a result of the different refractive index of the air from that of the solution the beam of light will be used to interrogate. As molecular binding events occur in solution, the refractive index changes that accompany these binding events will produce a further change in the relative phase of the two light beams and lead to a change in the generated fringe pattern as it appears at the CCD camera. These phase changes can be measured and used as an indication of binding events either in solution or at a surface. A calibration curve can be generated relating the relative phase changes observed to changes in the refractive index of the solution.

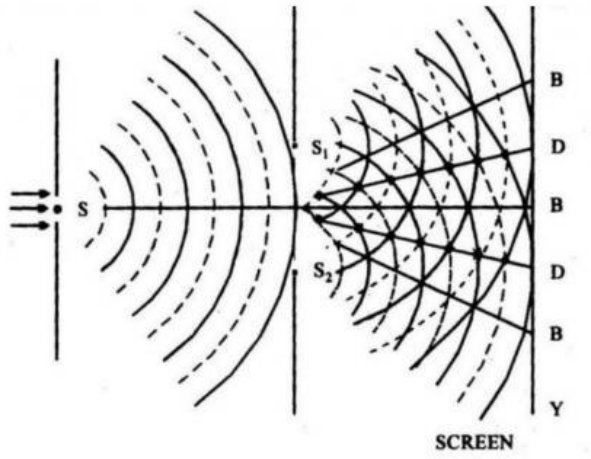

Figure 4.1 – Interference Fringe Patterns. This is a depiction of an interference fringe pattern produced by the double slit experimental arrangement. The image was adapted from reference 4.

In the backscattering interferometry arrangement, a small micro fluidic chamber is manufactured that allows for the reflection of light within the micro fluidic chamber many times. This allows the light beam to pass through sample with numerous passes and increases its effective path length leading to a higher sensitivity.[1] Figure 4.2 is an example of a typical experimental arrangement for the BSI instrumentation. In this arrangement, a laser source is focused onto mirror that reflects the beam into a micro fluidic chamber containing the sample

being analyzed. After undergoing multiple passes through the medium, the beam of light emerges from the sample and spatially overlaps with the incident beam of light so an interference pattern is generated due to the difference in phase between the incident light beam and that of the reflected light beam after passing through the sample. The interference fringe pattern is projected onto a CCD camera detector. The fringe pattern contains a dominant Fourier frequency; the phase of this dominant frequency is the BSI fringe shift signal, in radians.[2] Fourier analysis of this fringe pattern reports on very small changes in refractive index that can be correlated in real time with receptor-ligand interactions occurring in solution or with species tethered to the micro fluidic channel surface without the use of contrast-enhancing label molecules of any kind.[2] Spatial changes in interference fringes are measured in near real-time using high-resolution interference fringes and a fast Fourier transform FFT. In the general case, a Fourier transform is defined as equation 4.1

$$\boldsymbol{A(x) = F[a(y)] = a(y)e^{-i2fy}dy} \qquad \textbf{(4.1)}$$

In equation 4.1 A(x) is the complex Fourier transform of the function a(x), F[x] is the Fourier transform operation, y is a spatial variable and f is a spatial frequency in the Fourier domain.[2] For a given set of frequencies the calculation of the observed phase change is possible by evaluating the real and imaginary parts of the Fourier transform at a given frequency.[2] By applying this equation to the interference fringe data acquired in during BSI experiments it is possible to calculate the change in the phase shift due to changes in the refractive index of the solution.

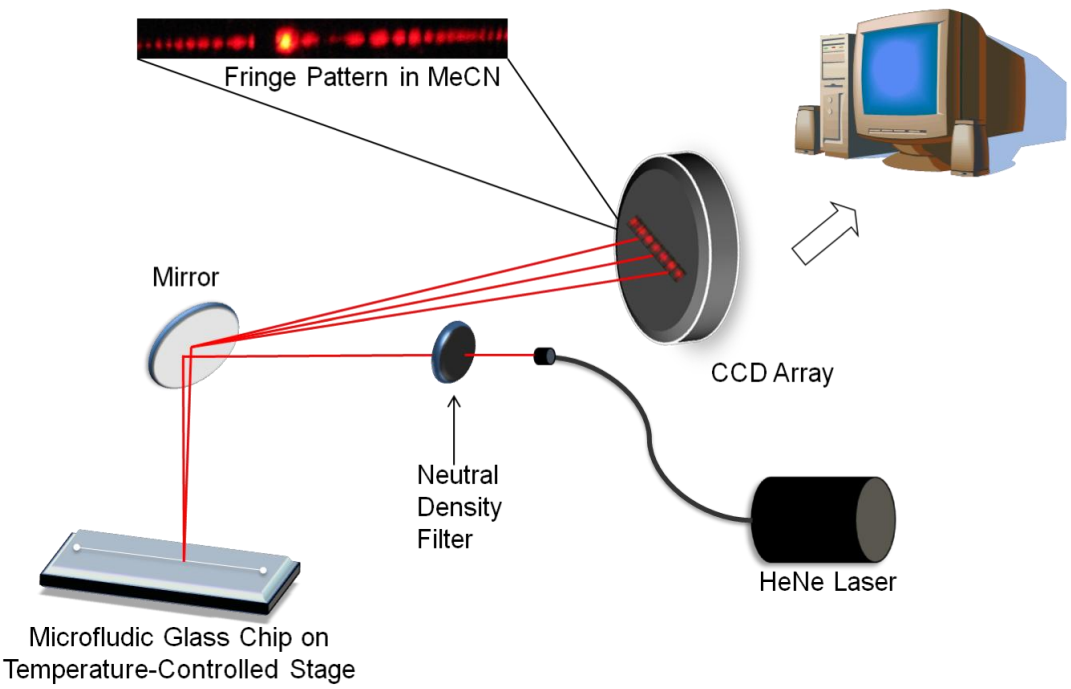

Figure 4.2 – Experimental Arrangement of a Typcial Backscattering Interferometer. This diagram illustrates the typical arrangement of instrumentation for a BSI experimental set up. The image is adapted from reference 1.

4.2 Materials and Methods

The backscattering interferometer was utilized in conjunction with supported lipid bilayer coated nanoparticles to evaluate the sensitivty of the BSI when coupled with plasmonic nanoparticles. Membrane encapsulated nanoparticles were produced according to the procedure in chapter 3. Cholera Toxin Subunit B was used as a model test system. Nanoparticles were synthesized according to the prodecure in chapter 2. The BSI instrumentation has been described previously by Dr. Michael Baksh of Georgia Tech who collaborated with us on these measurements.[2] Bovine Serum Albumin (BSA), Streptavidin Affinity Purified, lyophilized from 10mM Potassium Phosphate and 0.5mL centrifuge tubes were purchased from Sigma Aldrich. The following lipids were purchased from Avanti Polar Lipids (Alabaster, AL): 1,2-dioleoyl-sn-glycero-3-phosphocholine (DOPC). *Lyso*-Monosialoganglioside GM_1 (NH_4^+salt) was purchased from Matreya LLC (Pleasant Gap, PA). Cholera Toxin B subunit ≥95% (SDS-PAGE), lyophilized powder was purchased from Sigma Aldrich.

4.3 Backscattering Interferometry Measurements Using Nanocubes

In order to assess the lowest concentration of nanoparticles the BSI instrument is capable of detecting, a titration of nanoparticles was performed to evaluate the change in refractive index when various concentrations of supported lipid bilayer coated nanoparticles were exposed to cholera toxin subunit B at a constant concentration of 500nM. The supported lipid bilayer contained a constant GM1 composition of 1%. The goal here was to determine how small of a number of particles the BSI instrument is capable of detecting binding events at its surface. For comparison to the BSI's required particles concentration, the UV-Visible solution based spectroscopic measurements performed by Wu et al. used a concentration of approximately 1pM.[3] The effective concentration of nanoparticles, where binding events between Cholera Toxin Subunit B and GM1 at their surface were detectable, was explored using both a 632.8nm laser and a 440nm laser. These wavelengths correspond to the dipolar and quadrapolar LSPR modes of the nanocubes. The phase shifts determined at various nanocube concentrations using the 440nm laser and the 632.8nm laser when performing the above experiments, are shown in figures 4.3 and 4.4 respectively.

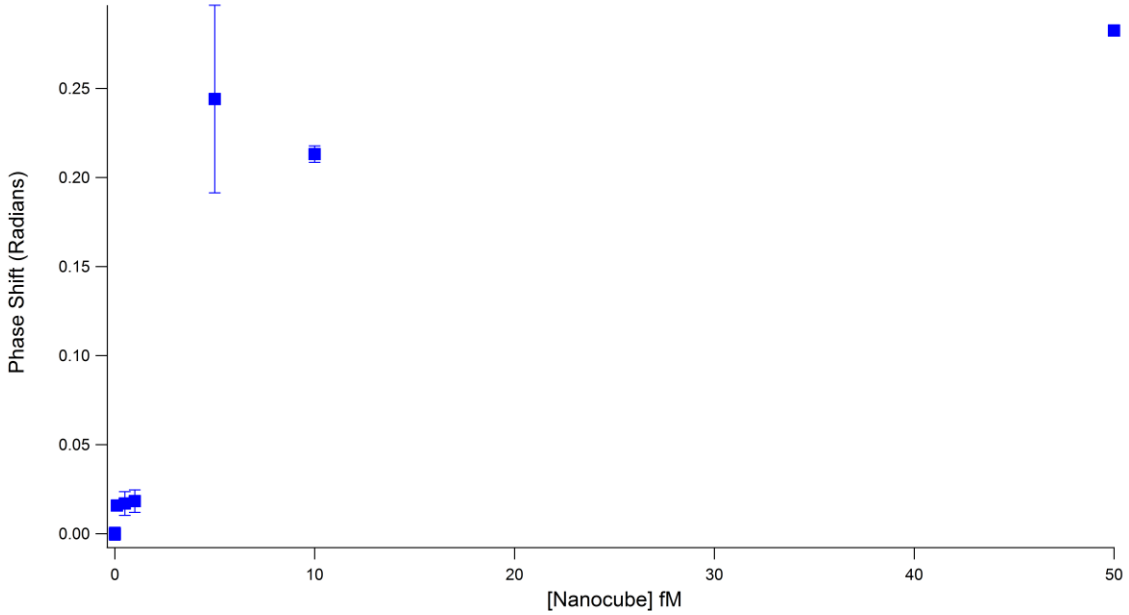

Figure 4.3 – Cholera Toxin Subunit B Binding to GM1 as a Function of Nanocube Concentration Using a 440nm Laser. This plot illustrates the response of the BSI to the number of particles used in the detection of the binding of Cholera Toxin Subunit B to GM1 in a supported lipid bilayer. A constant Cholera Toxin Subunit B concentration of 500nM is used for all data points. A 440nm laser was used for illumination. The y-axis illustrates the measured phase change for the binding of Cholera Toxin Subunit B.

.

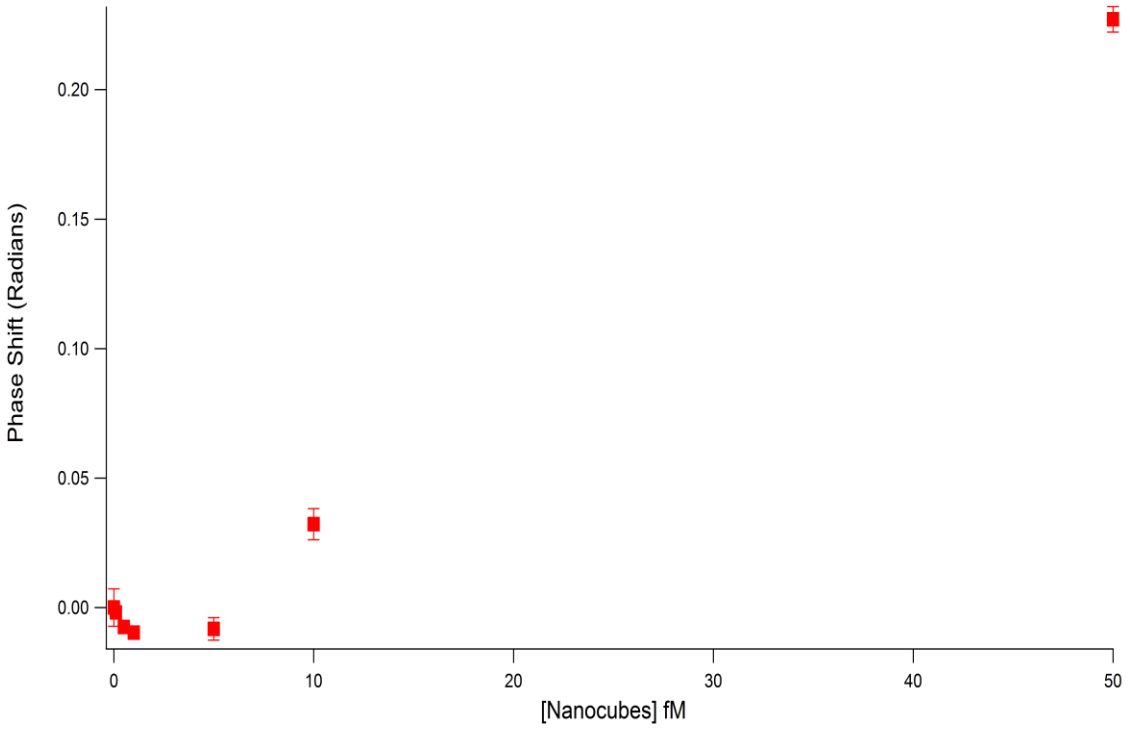

Figure 4.4 – Cholera Toxin Subunit B Binding to GM1 as a Function of Nanocube Concentration Using a 632.8nm Laser. This plot illustrates the response of the BSI instrument to the number of particles used in the detection of the binding of Cholera Toxin Subunit B to GM1 in a supported lipid bilayer. A constant Cholera Toxin Subunit B concentration of 500nM is used for all data points. A 632.8nm laser was used for illumination. The y-axis illustrates the measured phase change for the binding of Cholera Toxin Subunit B.

The nanocube titration at a 500nM Cholera Toxin Subunit B concentration shows that is the BSI capable of detecting Cholera Toxin Subunit B binding to GM1 receptors in supported lipid bilayer encapsulated nanoparticles, at concentrations in the low femtomolar range. This is a nanoparticle concentration that is 1000 times lower than that used in UV-Visible spectroscopy measurements.[3] In addition there appears to be a significant signal from the difference between the 632.8nm and 440nm laser arrangement for the BSI. This facet of the experiment is currently being further explored by Dr. Michael Baksh of Georgia Tech. Preliminary results suggest that the 440nm laser is capable of detecting binding of Cholera Toxin Subunit B to GM1 on membrane encapsulated nanoparticles in the 1-5fM range, while the 632.8nm laser does not detect binding until the 50fM range. This represents an addition 10 fold enhancement of the 440nm laser above the 632.8nm. The 440nm laser is probing the quadrapolar LSPR mode of the nanoparticles while the 632.8nm laser is probing the dipolar LSPR mode. As can be seen in figure 2.3, the quadrapolar LSPR mode has narrower full width at half maximum than the dipolar LSPR mode and hence has a much higher figure of merit as defined by equation 1.7.

The binding of Cholera Toxin Subunit B to supported lipid bilayer encapsulated nanoparticles with a constant 1% GM1 composition was explored in addition to determine the sensitivity of the BSI when using the nanoparticle based assay. This titration was performed using the red laser (λ=632.8nm). The exploration of the blue lasers (λ=440nm) effective enhancement of this binding curve assays sensitivity is something we shall explore in future experiments. The 632.8nm wavelength corresponds closely to the dipolar LSPR mode of the nanocube LSPR peak and we expect the results of the 440nm laser binding curve sensitivity to show an improvement over the minimum concentration of molecules necessary to produce a detectable signal from the BSI. This experiment will show that the incorporation of the nanoparticles into the BSI does indeed enhance the sensitivity of the instrument. To demonstrate this fact, we have performed a Cholera Toxin Subunit B binding curve titration on both SUVs and supported lipid bilayer coated nanoparticles. The lipid compositions of both the SUVS and nanoparticles consisted of 99% DOPC and 1% GM1. The concentration of nanoparticles used here was 10fM. The goal here was to determine the enhancement of the BSI sensitivity when measuring binding events at the nanoparticles surface relative to binding at the SUVs surface. It should be noted that the actual concentration of SUV was higher than that of the nanoparticles but the total number of GM1 binding sites was adjusted to be the same in both experiments.

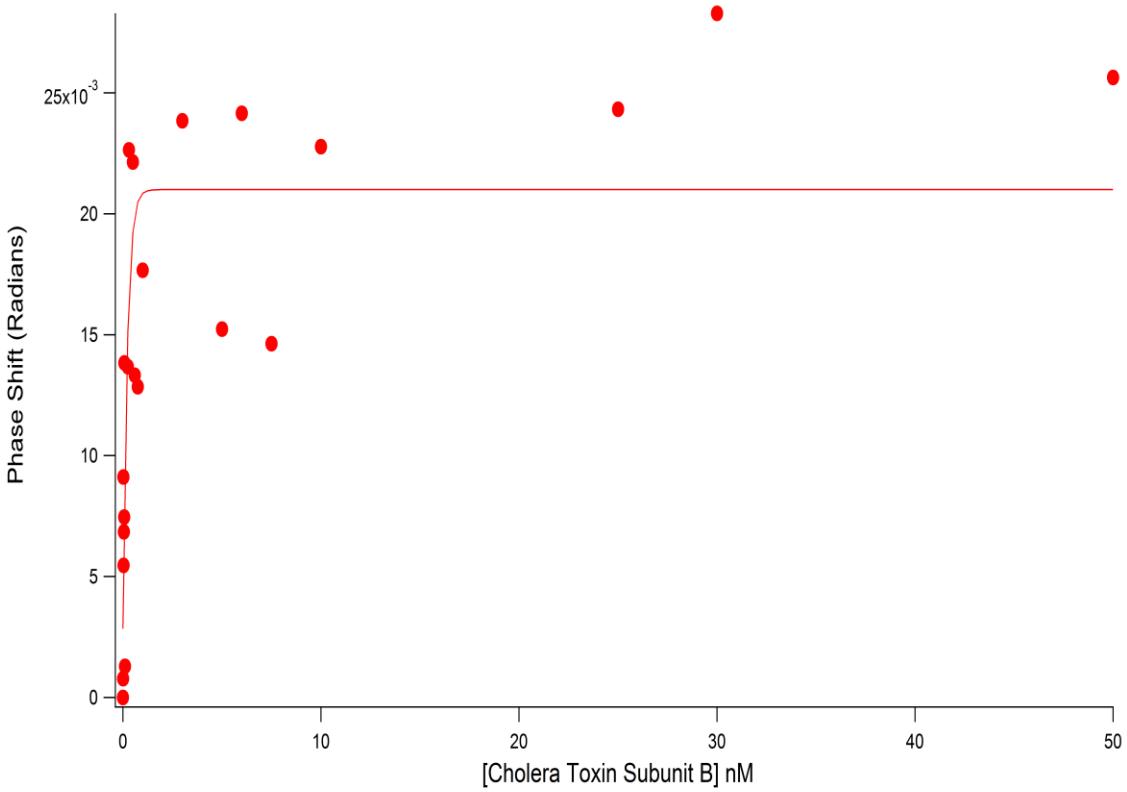

Figure 4.5 – BSI Titration Curve for Cholera Toxin Subunit B Binding to GM1 on Bilayer Encapsulated Nanoparticles. The titration was performed using membrane encapsulated nanoparticles with a lipid composition of 99% DOPC and 1% GM1.

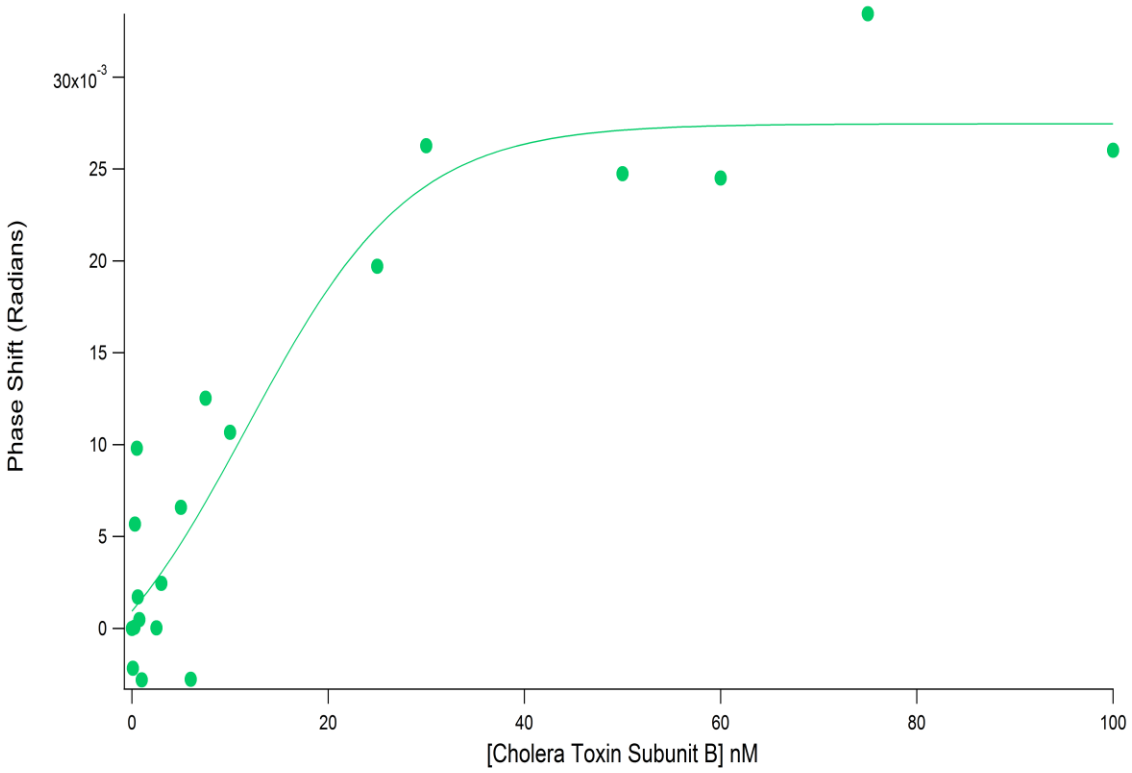

Figure 4.6 – BSI Titration Curve for Cholera Toxin Subunit B Binding to GM1 on SUVs. The titration of Cholera Toxin Subunit B binding to GM1 receptors was performed using single unilaminar vesicles (SUVs) with a lipid composition of 99% DOPC and 1% GM1.

The suggested enhancement of the BSI when used in conjunction with the nanoparticles sensitivity is seen in figure 4.5 and 4.6. As noted before, the concentration of nanoparticles necessary for nanoparticle binding measurements is significantly lower than for UV-Visible spectroscopy. In addition the number of SUVs used in the BSI measurements is also significantly higher than the actual number of particles present in solution. However, the phase shift, which is directly related to the mass change at the surface of the nanoparticles or SUVs respectively, is significantly higher at lower concentrations of Cholera Toxin Subunit B for the nanoparticle based BSI measurements in comparison to the SUV based measurements. At a Cholera Toxin Subunit B concentration of 0.01nM or 10pM, the nanoparticles register a phase change of 0.000778 radians, while the SUVs essentially show no change at all. The overall phase changes, for the nanoparticle-based measurements, are much higher at the low concentrations of Cholera Toxin Subunit B, when compared to the SUV-based measurements. This can be seen by comparing the magnitude of phase change at the low concentration range of Cholera Toxin Subunit B for the nanoparticle-based measurements to the SUV-based measurements shown in figures 4.5 and 4.6. The phase change is correlated to changes in refractive index of the solution due to binding events occurring at the surface of the SUVs and nanoparticles.[1] The preliminary improvements in the detection levels of the BSI using nanoparticles is very promising and an exciting area of exploration for improving the BSI's, already sensitive measurement abilities, as a solution-based, label-free detection method.

In addition to the increased sensitivity provided by incorporating plasmonic nanoparticles into the BSI instrument, the reduced number of particles required when using nanoparticles as an alternative to SUVs for membrane binding experiments is of additional benefit. The reduced number of particles required when coupled to the small volume of sample required, when using the BSI, will drastically reduce the amount of sample required to perform each measurement. This is a considerable factor when samples are very precious or difficult to obtain. The typical volume required in a BSI experiment is 1µL, so that even without the use of nanoparticles, this platform allows sensitive measurements to be performed with very little sample. Nanocube-based BSI measurements will reduce this sample requirement even further. The number of particles that are being interrogated in 1µL of sample, with a nanocube concentration of 10fM, corresponds to approximately 6000 nanoparticles in solution. If the enhancement factor seen when using the blue 440nm laser, which was capable of detecting binding events for Cholera Toxin Subunit B at a constant concentration of 500nM in a solution of 3fM nanoparticles, is taken into account, the number of particles drops to approximately 1800 when interrogating an identical volume of sample. In comparison, the UV-Visible spectroscopy measurements, that utilize a working concentration of cubes in the 1pM range with a volume of 10µL, amounts to approximately 6×10^6 nanoparticles. Clearly the number of particles needed in the BSI is orders of magnitude smaller than that required when working with solution-based measurements using a UV-Visible spectrophotometer. While further work is needed on the development of the BSI platform for use with

plasmonic nanoparticles, it is clear that the instrument is capable of proving to be a very sensitive, label-free, solution-based assay with an incredibly low number of particles required to observe binding events.

4.4 Literature References

1. Bornhop DJ, Latham JC, Kussrow A, Markov DA, Jones RD, Sorensen HS. Free-Solution, Label-Free Molecular Interactions Studied by Back-Scattering Interferometry. Science. 2007; 317:1732–1736. [PubMed: 17885132]
2. Baksh M.M, Kussrow A.K., Mauro Mileni M., Finn M.G., and Bornhop D.J. Nature Biotechnology. 2011 April; 29(4): 357–360
3. Wu H-J., Joel Henzie J., W-C., C., Z., E., J., P., J.T., Nature Methods 2012, 9, 1189–1191.
4. http://images.tutorvista.com/cms/images/95/double-slit-experiment.jpg

Bibliography

1. Wild D., *The Immunoassay Handbook,* 3rd ed, Elsevier, Amsterdam, **2005.** [general immunoassay information]
2. Diamandis E.P. and Christopoulos T.K. *Immunoassay*, Academic Press, Inc., San Diego, **1996***.*
3. Griffiths J., Analytical Chemistry, **2007**, 79, 8833.
4. Grassi J., Creminon C., Frobert Y., Etienne E., Ezan E., Volland H. and Pradelles P., Clinical Chemistry, **1996**, 42, 1532.
5. Selby, C., Annals of Clinical Biochemistry, **1999**, 36, 704 [Hook Effect]
6. Apple F.S., Murakami M.M., Christenson R.H., Campbell J.L., Miller C.J., Hock K.G. and Scott M.G., Clinica Chimica Acta, **2004**, 345, 123.
7. Willits K., Van Duyne R.P., Annual Review of Physical Chemistry, **2007,** 58, 267.
8. Chu F.S., Ekins R., *Protein Arrays, Biochips and Proteomics: The Next Phase of Genomic Discover*, Elsevier Amsterdam, 2003.
9. Hermanson G. *Bioconjugate Technicques, 3rd ed, Elsevier, Amsterdam, 2013.*
10. Adams, R., Bachman, W.E., Fieser, L.F., Johnson, J.R., and Snyder, H.R. (1942) *Organic Reactions*, Vol. 1, p. 303. Wiley, New York
11. Myszka D.G., Current Opinion in Biotechnology, **1997,** 8, 50.
12. Rich R.L. and Myszka D.G., Current Opinion in Biotechnology, **2000,** 11, 54.
13. Kyo M., Kazue U.-A., and Koga H., Analytical Chemistry, **2005,** 77, 7115.
14. Pattnaik P., Applied Biochemistry and Biotechnology, **2005**, 126, 79
15. Yonzon C.R., Jeoung E., Zou S., Schatz G.C., Mrksich M., Van Duyne R.P., Journal of American Chemical Society, **2004,** 126, 12669-12676.
16. Schatz GC, Young MA, Van Duyne R.P., **2006** pp. 19–46. Berlin: Springer-Verlag.
17. Kelly KL, Coronado E, Zhao L, Schatz G.C., Journal of Physical Chemistry B, **2003,** 107:668–77.
18. Bohren CF, Huffman DR., *Absorption and Scattering of Light by Small Particles*. Wiley, New York, 1983, 530 pp.
19. Mie G. *Ann. Phys., **1908,*** 25:377–445.
20. Link S, El-Sayed M.A., *J. Phys. Chem. B,* **1999,** 103:8410–26.
21. Draine BT, Flatau P.J., *J. Opt. Soc. Am. A,* **1994,** 11:1491–99
22. Jensen TR, Kelly KL, Lazarides A, Schatz GC., *J. Cluster Sci.,* **1999,** 10:295–317
23. Yang W., Schatz G.C., Van Duyne R.P., *J. Chem. Phys.,* **1995,** 103:869–75
24. Taflove A., *Computational Electrodynamics: The Finite-Difference Time Domain Method*. Boston: Artech House, 1995.

25. Novotny L., Bian R.X., Xie X.S., *Phys. Rev. Lett,* **1997,** 79:645–48
26. Bian R.X., Dunn R.C., Xie X.S., Leung P.T., *Phys. Rev. Lett.,* **1995,** 75:4772–75
27. Haes A.J., Van Duyne R.P., *J. Am. Chem. Soc.,* **2002,** 124:10596–604
28. Jung L.S, Campbell C.T., Chinowsky T.M., Mar M.N., Yee S.S., *Langmuir,* **1998,** 14:5636–48
29. Mayer K.M. and Hafner J.H, Chemical Review, **2011**, 111, 3828–3857
30. Smith EA, Corn RM. 2003.. *Appl. Spectrosc.,* **2003***,* 57:A320–22
31. Giebel K.F., Bechinger C., Herminghaus S., Riedel M., Leiderer P., et al., *Biophys. J.,* **1999,** 76:509–16
32. Berger C.E.H., Beumer T.A.M., Kooyman R.P.H., Greve J., *Anal. Chem.,* **1998,** 70:703–6
33. Tao A.R., Sinsermsuksakul P., Yang P., Angew.Chem., **2006**, 118, 4713–4717; Angew.Chem. Int. Ed., **2006**, 45, 4597
34. Sun Y., Xia Y., Science, **2002**, 298, 2176.
35. Wu H-J., Henzie J., W-C. Lin, Rhodes C., Li Z., Sartorel E., Thorner J., Yang P., Groves J.T., Nature Methods, **2012***,* 9, 1189–1191.
36. Stöber, W., Fink, A. & Bohn, E. *J. Colloid Interface Sci.,* **1968,** 26, 62–69.
37. Kim F., Connor S., Song H., Kuykendall T., Yang P., Angew. Chem., **2004,** 116, 3759 – 3763; Angew. Chem. Int. Ed., **2004,** 43, 3673.
38. Wiley B., Herricks T., Sun Y., Xia Y., Nano Lett., **2004,** 4, 1733.
39. Frenken J. W. M., Stoltze P., Phys. Rev. Lett., **1999,** 82, 3500.
40. Purcell E.M., Pennypacker C.R., Astrophys. J., **1973,** 361, 705.
41. Draine B.T., Flatau P.J., J. Opt. Soc. Am., **1994**, A11, 1491.
42. Sherry L.J., Chang S.-H., Wiley B.J., Xia Y., Schatz G.C., Van Duyne R.P., Nano Lett., **2005,** 5, 2034.
43. Fuchs R., Phys. Rev. B, **1975,** 11, 1732.
44. Kelly K.L., Coronado E., Zhao L.L., Schatz G.C., J. Phys. Chem. B, **2003,** 107, 668.
45. Freeman R.G., Grabar K.C., Allison K.J., Bright R.M., Davis J.A., Guthrie A.P., Hommer M.B., Jackson M.A., Smith P.C., Walter D.G., Natan M.J., Science, **1995,** 267, 1629.
46. Moskovits M., Rev. Mod. Phys., **1985,** 57, 783.
47. Iijima M. and Kamiya H., Powder and Particle Journal, **2009,** No.27
48. Dhanasekaran Kimberly, Zhang D.T., and Meisel D., J. Am. Chem. Soc., **2002,** 124, pp.2312-2317.
49. Verwey, E. J. W. and Overbeek, J., "Theory of the stability of lyophobic colloids", Elsevier Publishing Company, 1947.
50. Tao A.R., Yang P., J.Phys. Chem. B, **2005,** 109, 15, 687.
51. Song H., Kim F., Connor S., Somorjai G.A., Yang P., J. Phys. Chem. B, **2005,** 109, 188.
52. Kim F., Connor S., Song H., Kuykendall T., Yang P., Angewandte Chemie International Edition, **2004,** 43, 3673.
53. Zhou Y., Wang C.Y., Zhu Y.R., Chen Z.Y., Chem. Mater., **1999,** 11, 2310/
54. Chen S., Carroll D.L., Nano Lett., **2002,** 2, 1003.
55. Zhou .Y et al., Advanced Materials, **1999,** 11, 850.

56. Mackay A.L., Acta Crystallographica, **1962,** 15, 916.
57. Baletto F., Mottet C., Ferrando R., Physical Review B, **2001,** 63, 155408.
58. Ino S., Ogawa S., Taoka T., H. Akahori H., Japanese Journal of Applied Physics, **1972,** 11, 1859.
59. Marks L.D., Smith D.J., Journal of Crystal Growth, **1981,** 54, 425.
60. Baletto F., Ferrando R., Reviews of Modern Physics, **2005,** 77, 317.
61. Sun Y., Mayers B., Herricks T., Xia Y., Nano Lett., **2003**, 3, 955.
62. Johnson C.J., Dujardin E., Davis S.A., Murphy C.J., Mann S., Journal of Materials Chemistry, **2002,** 12, 1765.
63. Millstone J.E. *et al.*, *Journal of the American Chemical Society,* **2005,** 127, 5312.
64. Kumbhar A.S., Kinnan M.K., Chumanov G., *Journal of the American Chemical Society* **2005,** 127, 12444.
65. Sosa I.O., Noguez C., Barrera R.G., *J. Phys. Chem. B,* **2003,** 107, 6269.
66. Kawata S., *Topics Appl. Phys.,* **2001,** 81, 1.
67. Mock J.J., Barbic M., Smith D.R., Schultz D.A., Schultz S., *Journal of Chemical Physics,* **2002,** 116, 6755.
68. Fievet F., Lagier J.P., Blin B., Beaudoin B., Figlarz M., *Solid State Ionics*, **1989,** 198.
69. Frenken J.W.M., Stoltze P., *Physical Review Letters,* **1999,** 82, 3500.
70. Purcell E.M., Pennypacker C.R., *Astrophysical Journa,* **1973,** 361, 705.
71. Draine B.T., Flatau P.J., *Journal of the Optical Society of America,* **1994,** A11, 1491.
72. Sherry L.J. *et al.*, *Nano Letters,* **2005,** 5, 2034.
73. Fuchs R., *Physical Review B,* **1978,** 11, 1732.
74. Sannomiya T., Junesch J. and Prayanka Rajendran P. *Optical Imaging: Technology, Methods and Applications, Imaging, Spectroscopy and Sensing with Single and Coupled Metallic Nanoparticles,* 2012, Chapter
75. Zsigmondy R.; Alexander, J., *Colloids and the ultramicroscope; a manual of colloid chemistry and ultramicroscopy*, New York, John Wiley & Sons., 1909.
76. Mie; G., Ann. Phys., **1908,** 330, 377-445.
77. Hutter, E., Fendler J. H., Adv. Mater., **2004,** 16, 1685-1706.
78. Lakowicz, J. R., Plasmonics, **2006,** 1, 5-33.
79. Murray, W. A.; Barnes, W. L., Adv. Mater., **2007,** 19, 3771-3782.
80. Masson, J. F.; Murray-Methot, M. P.; Live L. S. (2010) Analyst 135, 1483-1489.
81. Hafner, C., *The Generalized Multipole Technique for Computational Electromagnetics*, Boston, Artech House. 1990.
82. Gans, R., Ann. Phys., **1912,** 342, 881-900.
83. Johnson, P. B., Christy, R. W., Phys. Rev. B, **1972,** 6, 4370-4379
84. Hafner, C., MaX-1: A Visual Electromagnetics Platform, Chichester UK, Wiley, 1998.
85. Sannomiya, T., Hafner, C., J. Comput. Theor. Nanosci, **2010,** 7, 1587-1595.
86. Okamoto T. Yamaguchi I., Kobayashi T., Opt. Lett, **2000,** 25, 372-374.

87. Nordlander, P.; Oubre, C.; Prodan, E.; Li, K.; Stockman, M. I., Nano Lett. 4, **2004,** 899-903.
88. Sannomiya, T.; Vörös, J., Trends in Biotechnology, **2011,** 29, 343-351.
89. Romero, I.; Aizpurua, J.; Bryant, G. W.; García de Abajo, F. J., Opt.Express, **2006,** 14, 9988-9999.
90. Zuloaga, J.; Prodan, E.; Nordlander, P., Nano Lett., **2009,** 9, 887-891.
91. Su K.-H., Wei Q.-H., Zhang X., Mock J.J., Smith D.R., Schultz S., Nano Lett., **2003** 3, 1087-1090.
92. Acimovic S.S., Kreuzer M.P., Gonzalez M.U., Quidant R., ACS Nano, **2003** 3, 1231-1237.
93. Rechberger W., Hohenau A., Leitner A., Krenn J.R., Lamprecht B., Aussenegg F.R., Optics Commun., **2003,** 220, 137-141.
94. Schneckenburger H., Curr. Opin. Biotech, **2005,** 16, 13-18.
95. Dahlin A. B., Tegenfeldt J. O., Hook F., Anal. Chem., **2006,** 78, 4416-4423.
96. Curry A., Nusz G., Chilkoti A., Wax A., Appl. Opt., **2007,** 46, 1931-1939.
97. Knight, M. W.; Wu, Y.; Lassiter, J. B.; Nordlander, P.; Halas, N. J., Nano Lett., **2009,** 9, 2188-2192.
98. Hu M., Novo C., Funston A., Wan H., Staleva H., Zou S., Mulvaney P., Xiae Y., and Hartland G.V., Journal of Material Chemistry, **2008**, 18, 1949–1960 | 1949
99. Van de Hulst H.C., Light Scattering by Small Particles, Dover Publications, New York, 1981.
100. Bohren C.F., Huffman D.R., *Absorption and Scattering of Light by Small Particles*. Wiley, New York. 530 pp., 1993.
101. Sonnichsen C., Geier S., Hecker N.E., Von Plessen G., Feldmann J., H. Ditlbacher , B. Lamprecht, J. R. Krenn, F. R. Aussenegg, V. Z. H. Chan, J. P. Spatz and M. Moller, Appl. Phys. Lett., **2000**, 77, 2949.
102. Schultz S., Smith D.R., Mock J.J., and Schultz D.A., Proc. Natl. Acad. Sci. U. S. A., **2000**, 97, 996.
103. Sonnichsen C., Franzl T., Wilk T., Von Plessen T.G., Feldmann J., Wilson O. and Mulvaney P., Phys. Rev. Lett., **2002**, 88, 077402.
104. Mock J., Barbicm M., Smith D.R., Schultz D.A., and Schultz S., J. Chem. Phys., **2002**, 116, 6755.
105. Kuziemko G.M., Stroh M., and Stevens R.C., *Biochemistry,* **1996,** *Vol. 35, No. 20.*
106. Shi J., Yang T., Kataoka S., Zhang Y., Diaz A.J., and Cremer P.S., Journal of American Chemical Society, **2007** 129(18): 5954–5961
107. Wu H-J., Henzie J., W-C. Lin, Rhodes C., Li Z., Sartorel E., Thorner J., Yang P., Groves J.T., Nature Methods **2012***,* 9, 1189–1191.
108. Sherry L.J., Chang S-H., Wiley B.J., Xia Y., Schatz G.C., and Van Duyne R.P., Nano Lett., **2005,** 5, 2034-2038.
109. Malinsky M.D., Kelly K.L., Schatz G.C., Van Duyne R.P., *J. Am. Chem. Soc.,* **2001,** 123:1471–82.
110. Jung L.S., Campbell C.T., Chinowsky T.M., Mar M.N., Yee S.S., *Langmuir,* **1998,** 14:5636–48.

111. Smith E.A., Corn R.M., *Appl. Spectrosc.,* **2003,** 57:A320–22.
112. Brockman J.M., Nelson B.P., Corn R.M., *Annu. Rev. Phys. Chem.,* **2000,** 51:41–63.
113. Giebel K.F., Bechinger C., Herminghaus S., Riedel M., Leiderer P., et al., *Biophys. J.,* **1999,** 76:509–16.
114. Berger C.E.H., Beumer T.A.M., Kooyman R.P.H., Greve J., *Anal. Chem.,* **1998,** 70:703–6.
115. Endo T., Kerman K., Nagatani N., Takamura Y., Tamiya E., *Anal. Chem.,* **2005,** 77:6976–84.
116. Endo T., Yamamura S., Nagatani N., Morita Y., Takamura Y., Tamiya E., *Sci. Technol. Adv. Mater.,* **2005,** 6:491–500.
117. Kik P.G., Maier S.A., Atwater H.A., *Proc. SPIE,* **2004,** 5347:215–23.
118. Sundaramurthy A., Schuck P.J., Conley N.R., Fromm D.P., Kino G.S., Moerner W.E., *Nano Lett.,* **2006,** 6:355–60.
119. Malmqvist M., *Nature,* **1993,** 361:186–87.
120. Van Duyne R.P., *Science,* **2004,** 306:985–86.
121. Knoll W., *Annu. Rev. Phys. Chem.,* **1998***,* 49:569–638.
122. Haes A.J., Van Duyne R.P., *Anal. Bioanal. Chem.,* **2004,** 379:920–30.
123. Haes A.J., Haynes C.L., McFarland A.D., Zou S., Schatz G.C., Van Duyne R.P., *MRS Bull,* **2005,** 30:368–75.
124. Englebienne P., *Analyst,* **1998,** 123:1599–603.
125. Raschke G., Kowarik S., Franzl T., Soennichsen C., Klar T.A., et al. ,*Nano Lett.,* **2003,** 3:935–38.
126. Srituravanich W, Fang N, Sun C, Luo Q, Zhang X., *Nano Lett.,* **2004,** 4:1085–88.
127. Bornhop D.J., Latham J.C., Kussrow A., Markov D.A., Jones R.D., Sorensen H.S., Science, **2007;** 317:1732–1736. [PubMed: 17885132]
128. Baksh M.M, Kussrow A.K., Mauro Mileni M., Finn M.G., and Bornhop D.J. Nature Biotechnology**, 2011,** April; 29(4): 357–360
129. Wu H-J., Henzie J., W-C. Lin, Rhodes C., Li Z., Sartorel E., Thorner J., Yang P., Groves J.T., Nature Methods, **2012***,* 9, 1189–1191.
130. Kussrow, A.; Kaltgrad, E.; Wolfenden, M. L.; Cloninger, M. J.;Finn, M. G.; Bornhop, D. J. Anal. Chem. **2009**, 81, 4889–4897
131. Kussrow A., Enders C.S., and Bornhop D.J. Anal. Chem**. 2012**, 84, 779–792
132. Markov D.A., Swinney K., Bornhop D.J., J Am Chem Soc. **2004**, 126:16659–16664.
133. Rich R.L., Day Y.S.N., Morton T.A., Myszka D.G., Anal. Biochem., **2001,** 296, 197.
134. Markov D.A., Swinney K., Bornhop D.J., J. Am. Chem. Soc., **2004,** 126, 16659.
135. Latham J.C., Markov D.A., Sorensen H.S., Bornhop D.J., Angew. Chem. Int. Ed., **2006,** 45, 955.
136. Brosinger F., et al., Sens. Actuators B Chem., **1997,** 44, 350.
137. Prieto F., et al., Nanotechnology, **2003,** 14, 907.
138. Prieto F., et al., Sens. Actuators B Chem., **2003,** 92, 151.

139. Swinney K., Markov D., Bornhop D.J., Rev. Sci. Instrum., **2000**, 71, 2684.
140. Tarigan H.J., Neill P., Kenmore C.K., Bornhop D.J., Anal. Chem., **1996,** 68, 1762.
141. Sorensen H.S., Thesis, Technical University of Denmark, 2006.
142. Sorensen H.S., Larsen N.B., Latham J.C., Bornhop D.J., Andersen P.E., Appl. Phys. Lett, **2006,**. 89, 151108.
143. Swinney K., Markov D., Bornhop D.J., Anal. Chem., **2000,** 72, 2690.
144. Markov D.A., Dotson S., Wood S., Bornhop D.J., Electrophoresis, **2004,** 25, 3805.
145. Sonnino S, Mauri L, Chigorno V, Prinetti A., Glycobiology. **2007**; 17:1R–13R.
146. Fishman PH, Pacuszka T, Orlandi PA., Adv. Lipid Res. **1993**; 25:165–187.
147. Kuziemko G.M., Stroh M., Stevens R.C., Biochemistry, **1996**; 35:6375–6384.
148. Fang Y, Frutos A, Lahiri J., Langmuir. **2003**; 19:1500.
149. Cannon B, Weaver N, Pu Q, Thiagarajan V, Liu S, Huang J, Vaughn MW, Cheng KH., Langmuir**. 2005**; 21:9666–9674.
150. Brian A.A., McConnell H.M., Proc Natl Acad Sci USA. **1984,** 81:6159–6163.
151. Mossman K.D., Campi G., Groves J.T., Dustin M.L., Science. **2005**; 310:1191–1193.
152. Kussrow AK, Enders CS, Castro AR, Cox DL, Ballard RC, Bornhop D.J., Analyst. **2010**; 135:1535–1537.
153. Bornhop, D. J. *Appl. Opt.* **1995***, 34*, 3234-3239.
154. Born, M.; Wolf, E. In Principles of Optics: electromagnetic theory of propagation, interference and diffraction of light; Cambridge University Press: Cambridge, **1999**, pp 952.
155. Swinney, K.; Markov, D.; Hankins, J.; Bornhop, D. J. *Analytica Chimica Acta* **1999***, 40*0, 265-280.
156. Markov, D.; Begari, D.; Bornhop, D. J. *Anal. Chem.* **2002***, 7*4, 5438-5441.
157. Markov, D. A.; Swinney, K.; Norville, K.; Lu, D.; Bornhop, D. J. *Electrophoresis* **2002***, 2*3, 809-812.
158. Swinney, K.; Bornhop, D. J. *Analyst* **2000***, 12*5, 1713-1717.
159. Gilli, R.; Lafitte, D.; Lopez, C.; Kilhoffer, M.; Makarov, A.; Briand, C.; Haiech, J. *Biochemistry* **1998***, 3*7, 5450-5456.